Aorta-on-a-chip reveals impaired mitochondrial dynamics as a therapeutic target for aortic aneurysm in bicuspid aortic valve disease

Mieradilijiang Abudupataer[1], Shichao Zhu[1], Shiqiang Yan[2], Kehua Xu[2], Jingjing Zhang[2], Shaman Luo[2,3], Wenrui Ma[1], Md. Fazle Alam[2,3], Yuyi Tang[2], Hui Huang[2], Nan Chen[1], Li Wang[2], Guoquan Yan[2], Jun Li[1], Hao Lai[1], Chunsheng Wang[1] *, Kai Zhu[1] *, Weijia Zhang[1,2,3] *

[1] Department of Cardiac Surgery and Shanghai Institute of Cardiovascular Diseases, Zhongshan Hospital, Fudan University, Shanghai 200032, China; [2] Institutes of Biomedical Sciences, Shanghai Medical College, Fudan University, Shanghai 200032, China; [3] The State Key Laboratory of Molecular Engineering of Polymers, Fudan University, Shanghai 200438, China.

To whom correspondence should be addressed: Kai Zhu, Chunsheng Wang & Weijia Zhang

Emails: zhu.kai1@zs-hospital.sh.cn; wangchunsheng@fudan.edu.cn; weijiazhang@fudan.edu.cn

Keywords: organ-on-a-chip, thoracic aortic aneurysm, bicuspid aortic valve, mitochondrial dynamics, human aortic smooth muscle cells

Abstract

Background: Bicuspid aortic valve (BAV) is the most common congenital cardiovascular disease in general population and is frequently associated with the development of thoracic aortic aneurysm (TAA). There is no effective strategy to intervene with TAA progression due to an incomplete understanding of the pathogenesis. Insufficiency of NOTCH1 expression is highly related to BAV-TAA, but the underlying mechanism remains to be clarified.

Methods: A comparative proteomics analysis was used to explore the biological differences between non-diseased and BAV-TAA aortic tissues. A microfluidics-based aorta-on-a-chip model was constructed to evaluate the effect of NOTCH1 deficiency on contractile phenotype and mitochondrial dynamics of human aortic smooth muscle cells (HAoSMCs).

Results: Protein analyses of human aortic tissues showed the insufficient expression of NOTCH1 and impaired mitochondrial dynamics in BAV-TAA. HAoSMCs with NOTCH1-knockdown exhibited reduced contractile phenotype and were accompanied by attenuated mitochondrial fusion. Furthermore, we identified that mitochondrial fusion activators (leflunomide and teriflunomide) or mitochondrial fission inhibitor (Mdivi-1) partially rescued the disorders of mitochondrial dynamics in HAoSMCs derived from BAV-TAA patients.

Conclusions: The aorta-on-a-chip model simulates the human pathophysiological parameters of aorta biomechanics and provides a platform for molecular mechanism studies of aortic disease and related drug screening. This aorta-on-a-chip model and human tissue proteomic analysis revealed that impaired mitochondrial dynamics could be a potential therapeutic target for BAV-TAA.

Funding: National Key R&D Program of China, National Natural Science Foundation of China, Shanghai Municipal Science and Technology Major Project, Shanghai Science and Technology Commission, and Shanghai Municipal Education Commission.

Introduction

Bicuspid aortic valve (BAV) disease is the most common congenital cardiovascular abnormality and is found in nearly 1.4% of the general population (***Garg et al., 2005; Michelena et al., 2011; Verma and Siu, 2014***). BAV arises from incomplete separation or fusion of the aortic valve cusps and is associated with an approximately 40% risk of developing thoracic aortic aneurysm (TAA), namely, bicuspid aortopathy (***Verma and Siu, 2014***). BAV-TAA poses a severe health threat to a large population because progressive aneurysmal dilation can potentially develop into lethal dissection or rupture (***Goldfinger et al., 2014; Olsson et al., 2006***). The current clinical management mainly relies on prophylactic surgical repair of the notably dilated aorta (***Coady et al., 2010***). At present, the understanding of pathophysiological mechanisms of BAV-TAA is incomplete, which leads to the absence of effective pharmaceutical therapy to alleviate aortopathy progression (***Lindeman and Matsumura, 2019***). Multiple factors, such as genetics and haemodynamics, are involved in the etiologies of BAV-TAA. In particular, genetic factors are considered to play a pivotal role in the disease progression (***Isselbacher et al., 2016; Prakash et al., 2014***). NOTCH1 insufficiency has been observed in the population with BAV (***Balistreri et al., 2018; Harrison et al., 2019; Malashicheva et al., 2020; Sciacca et al., 2013***). However, the underlying mechanism through which insufficient NOTCH1 induces aortopathy remains to be explored.

Mitochondrial dysfunction has been closely linked to a variety of cardiovascular disorders, such as heart failure and atherosclerosis. Recent studies found that mitochondrial dysfunction was also related to the development of arterial aneurysm formation (***Cooper et al., 2020; van der Pluijm et al., 2018; Oller et al., 2021***). A single-cell transcriptome analysis on aneurysmal human aortic tissue suggested that mitochondrial dysfunction and increased chromatin oxidative phosphorylation (OXPHOS) were found in TAA tissues and insufficient ATP production might not be sufficient for the contractile activities of human aortic smooth muscle cells (HAoSMCs) (***Li et al., 2020***). Particularly, mitochondrial fission and fusion are dynamically balanced to maintain mitochondrial homeostasis and functions; and a shift towards fission event is one of the main causes of mitochondrial dysfunction. In a mice model of abdominal aortic aneurysm (AAA), impaired mitochondrial dynamics was found to play salient roles in disease development, and could be attenuated by the mitochondrial fission inhibitor Mdivi1 (***Cooper et al., 2020***). However, these studies focused on the analysis of abdominal aortic aneurysms and genetic TAA with FBN1 or Fubulin-4 mutation. It has been reported that there was close interaction between NOTCH1 signaling and homeostatic mitochondrial dynamics in the differentiation of cardiomyocytes (***Kasahara et al., 2013***) and the survival of breast cancer cells (***Chen et al., 2018***). Therefore, the relationship between NOTCH1 signaling pathway and mitochondrial dynamics in BAV-TAA needs to be clarified.

The traditional TAA animal models are frequently applied for the pathogenesis research and pharmaceutical therapy, however, not suitable for studying BAV-TAA. Although Koenig et al. generated NOTCH1-haploinsufficient mice in a preliminary 129S6 background that exhibited aortic root dilation, these mice did not show BAV characteristics (***Koenig et al., 2017***). Therefore, these models may not provide sufficient information of pathogenesis and drug response of BAV-TAA. Owing to the bioengineering advance, microfluidic-based organ-on-chip models have been widely developed to replicates human tissue microenvironment for toxicity analysis, drug screening and disease modeling and thus promotes pharmaceutical translation from preclinical studies to clinical trials (***Zhang et al., 2018; Ingber, 2016; Park et al., 2019; Thacker et al., 2020; Hofemeier et al., 2021***). It provides an opportunity to use a novel platform to study BAV-TAA on a susceptible human genetic background and may fill the gap between animal and human medicine. Here, we engineered an *in vitro* organ-on-a-chip model of primary HAoSMCs that emulates the biomechanics of the human aortic wall. We characterized the association between mitochondrial dynamics and NOTCH1 deficiency in BAV-TAA on this platform. Our study provides the first demonstration previously undocumented role of impairment of mitochondrial fusion in bicuspid aortopathy, which may serve as a potential pharmacological target for preventing disease progression.

Results

The relationship between NOTCH1 insufficiency and mitochondrial dysfunction in human TAA

To explore the pathological process involved in BAV-TAA, aortic tissues were collected from six patients with BAV-TAA who underwent ascending aorta replacement and six patients with non-diseased aorta who underwent cardiac surgery. The clinical characteristics of the patients are shown in ***Supplementary File-Table I***. Hematoxylin and eosin (H&E) staining showed interrupted elastic fibers and thinning of the tunica media in the BAV-TAA aortas compared with non-diseased aortic tissue (***Figure 1a***). A Western blotting analysis showed that NOTCH1 expression was significantly lower in BAV-TAA aortic tissues than in non-diseased aortic tissues. SM22 and CNN1 expression was significantly reduced in BAV-TAA aortic tissues (***Figure 1b-c***). We evaluated the expression of mitochondrial fission- and fusion-related proteins in non-diseased and BAV-TAA aortic tissues. The results showed that DRP1 and MFF expression was increased in the BAV-TAA group compared with the non-diseased group, but the differences were not significant probably due to individual patient differences, which resulted in relatively large protein expression differences within each group. However, the protein expression of MFN1 and MFN2 was significantly lower in the BAV-TAA group than in the non-diseased group (***Figure 1c***). In general, we found that MFN1 and MFN2 were expressed at low levels in tissues with NOTCH1 insufficiency (***Figure 1d***). The expression of NOTCH1 exhibited a positive correlation with MFN1 and MFN2 in aortic tissues. The expressions of DRP1 and MFF did not show a correlation with the expression of NOTCH1 (***Figure 1e***).

To further explore the biological differences between non-diseased and BAV-TAA aortic tissues, a comparative proteomics analysis of global proteins in aortic tissues was performed by high-performance liquid chromatography tandem mass spectrometry. In total, 70 upregulated proteins and 257 downregulated proteins were identified (***Supplementary File-Table II***). The enriched canonical pathways identified by Ingenuity Pathway Analysis (IPA) showed that acute phase response signaling, mitochondrial dysfunction and oxidative phosphorylation pathways were significantly enriched in BAV-TAA aortic tissues (***Figure 1f, Supplementary File-Table III***). In addition, metabolic signaling pathways affecting mitochondrial function, such as the EIF2 and sirtuin signaling pathways, were also significantly enriched in BAV-TAA. ***Figure 1g*** and ***Supplementary File-Table III*** show the enriched proteins associated with mitochondrial dysfunction, oxidative phosphorylation pathways, and acute phase response signaling. In total, seven upregulated proteins and 11 downregulated proteins were found to be related to acute phase response signaling, and 1 upregulated protein and 10 downregulated proteins were associated with mitochondrial dysfunction (***Figure 1g, Supplementary File-Table IV***). ***Figure 1h*** shows a volcano plot of these 11 differentially expressed proteins that allows visualization of the fold change and p-value of all differentially expressed proteins between the two groups. MFN1, MFN2, and NOTCH1 were not detected by mass spectrometry analysis, mainly because the aortic tissues contain highly cross-linked extracellular matrix that can be refractory to protein extraction. The publicly available data of the most compressive clinical aortic proteome, up to now, also indicated the missingness of MFN1, MFN2, DRP1 and NOTCH1 protein in aortic specimens (***Herrington et al., 2018***).

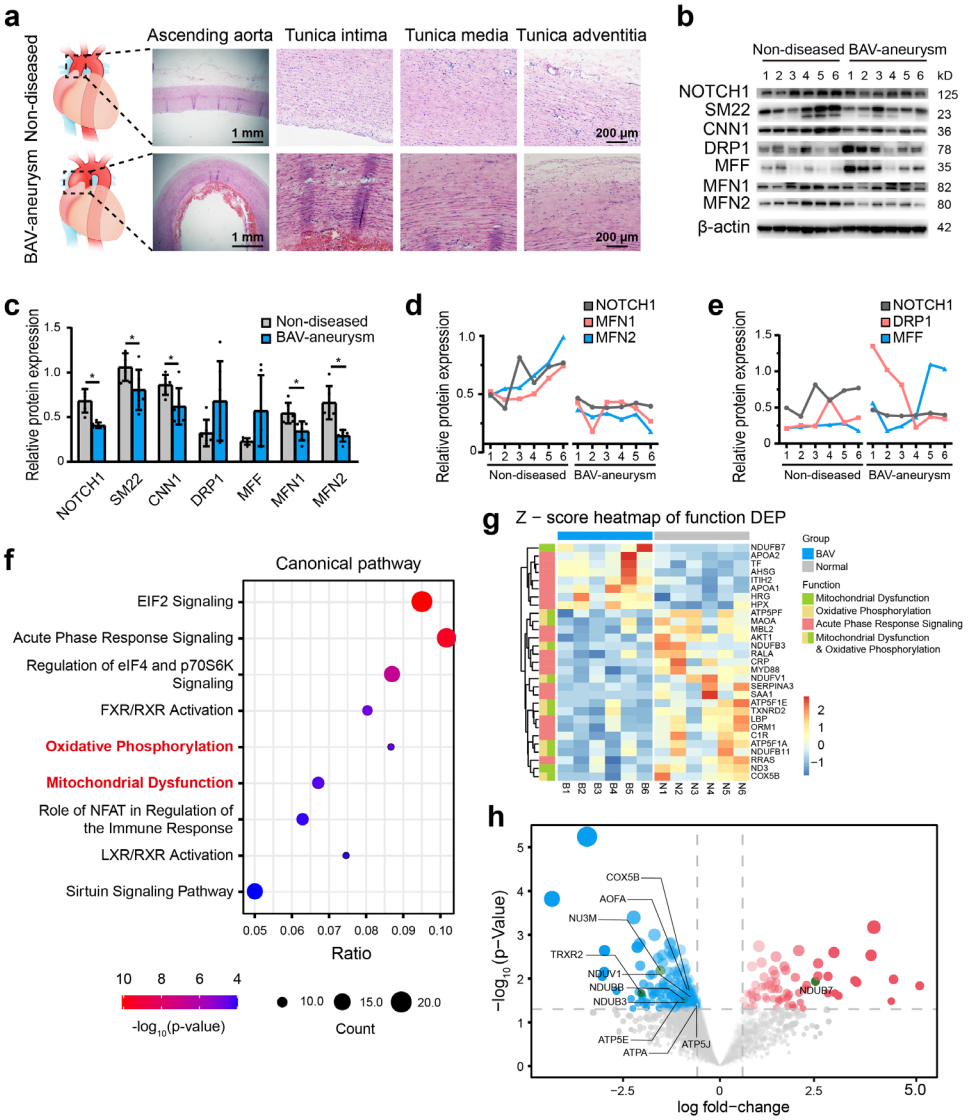

Figure 1. The relationship between NOTCH1 insufficiency and mitochondrial dysfunction in BAV-TAA. (**a**) H&E staining of non-diseased and BAV-TAA aortic tissues. The scale bar represents 1 mm in the low field and 200 μm in the high field. (**b**) Representative images of the western blotting analysis of the expression of NOTCH1, the mitochondrial dynamics proteins DRP-1, MFF, MFN1, and MFN2 and the contractile phenotype proteins SM22 and CNN1 in six non-diseased and six BAV-TAA aortic tissue fragments. (**c**) Quantification of the total band densities of the proteins normalized to the corresponding band density of β-actin (n = 6, $*P < 0.05$, two-tailed Student's t tests were used between two groups). (**d**) Correlation analysis among the quantified protein expression levels of NOTCH1, MFN1 and MFN2. A positive correlation was found between NOTCH1 and MFN1 or MFN2 in aortic tissues. The R^2 between NOTCH1 and MFN2 was 0.8069, and that between NOTCH1 and MFN1 was 0.6137. (**e**) Correlation analysis between the quantified protein expression of NOTCH1 and DRP1 or MFF. No correlation was found. (**f**) The enriched canonical pathways were identified by IPA. Mass spectrometry-based comparative proteomics showed that mitochondrial dysfunction and the oxidative phosphorylation pathways were significantly enriched in BAV-TAA aortic tissues. (**g**) Heatmap of the expression of enriched proteins involved in mitochondrial dysfunction, the oxidative phosphorylation pathways and acute phase response signaling. (**h**) Volcano plot visualization of the differentially expressed proteins related to mitochondrial dysfunction. The colors indicate the following: gray, no differential expression; red, upregulated proteins; and blue, downregulated proteins. The proteins related to mitochondrial dysfunction are labeled. All the data are expressed as the means ± SDs.

The online version of this article includes the following source data for figure 1:
Source data 1. The original raw data for western blotting.
Source data 2. List of total differential protein expression between non-diseased and BAV-TAA aortic tissues.
Source data 3. The total enriched canonical pathways in BAV-TAA aortic tissues.
Source data 4. List of total protein expression between non-diseased and BAV-TAA aortic tissues.

Construction of aorta-on-a-chip model

During cardiac systolic and diastolic cycles, the thoracic aortic wall experiences rhythmic tensile strain. Previous clinical studies have shown that the circumferential strains of the aortic wall range from low values of 7.0 ± 2.5% to high values of 21.5 ± 12.4%, and these can be further influenced by age, the aortic diameter, and the presence of aortopathy(***Akazawa et al., 2016; Bell et al., 2014***). To better simulate the rhythmic tensile strain experienced by HAoSMCs *in vivo*, we developed a compact microfluidic aorta-on-a-chip model with commercialized highly flexible polydimethylsiloxane (PDMS) membranes (***Figure 2a***). The model was composed of three chambers: i) a top vacuum chamber deforming the upper PDMS membrane; ii) a middle chamber containing the culture medium to maintain cell growth on the PDMS membranes; and iii) a bottom vacuum chamber deforming the lower PDMS membrane. HAoSMCs were cultured on the PDMS membranes in the middle cell culture chamber. The dimensions of the model are shown in ***Figure 2—figure supplement 1a***. Young's modulus of the commercialized PDMS membrane shows excellent homogeneity and tensile properties (***Figure 2—figure supplement 1b***). The rhythmic tensile strain was generated by connecting the top and bottom chambers to a vacuum pump that cyclically deformed the PDMS membrane. The rhythm and value of the dynamic negative pressure in the chambers were controlled by a set of apparatuses consisting of a monochip computer, a pressure regulator and a solenoid valve.

To quantify the tensile strains of the PDMS membrane generated by negative pressure in a vacuum chamber, we captured the real-time deformations of the PDMS membranes and measured the changes in length. With vacuum pressures of 0 kPa, 10 kPa, and 15 kPa, the dynamic deformations of the PDMS membranes were recorded from a cross-sectional view of the microfluidic model (***Figure 2b***). The two deformations of the upper and lower PDMS membranes were coincident in terms of amplitudes and rhythms (***Figure 2c***). A vacuum pressure of 10 kPa induced 7.18 ± 0.44% strain (7.09 ± 0.18% strain in the lower layer and 7.27 ± 0.28% strain in the upper layer), and 15 kPa induced 17.28 ± 0.91% strain (17.29 ± 0.62% strain in the lower layer and 17.23 ± 0.64% strain in the upper layer) (***Figure 2c and Figure 2—figure supplement 1c***). To replicate different strains on the human aortic wall, we applied 7.18 ± 0.44% strain induced by a vacuum pressure of 10 kPa as a relatively low strain and 17.28 ± 0.91% strain induced by a vacuum pressure of 15 kPa as a relatively high strain.

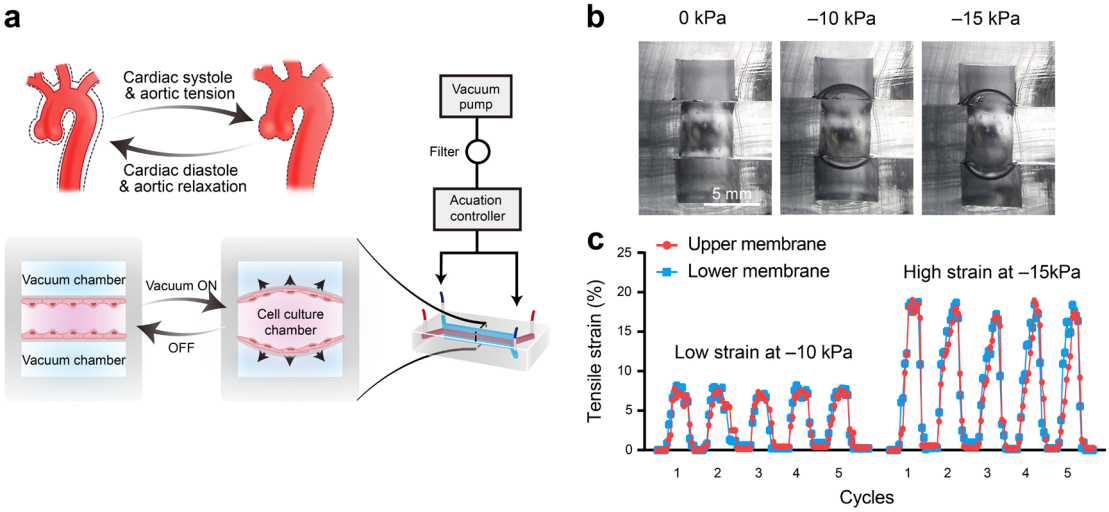

Figure 2. Schematic design and strain characterization of the aorta-on-a-chip model. (**a**) Schematic overview of the in vitro chip model. (**b**) Cross-sectional view of the microfluidic aorta-on-a-chip model showing the deformations of the PDMS membranes under different vacuum pressures. The scale bar represents 5 mm. (**c**) Measured tensile strains of the upper (red) and lower (blue) membranes at negative pressures of 10 kPa and 15 kPa for five cycles. The peak tensile strain per cycle averaged 7.18 ± 0.44% with a cyclic negative pressure of 10 kPa and 17.28 ± 0.91% with a cyclic negative pressure of 15 kPa.

The online version of this article includes the following figure supplement(s) and source data for figure 2:
Figure supplement 1. Characterization and parameters of the aorta-on-a-chip model.
Source data 1. The raw data of PDMS membrane Young's modulus.
Source data 2. The quantification data for measurement of tensile strains of the upper and lower membranes.

Rhythmic tensile strain defines cell alignment and enhances cell contractility

To identify the effect of rhythmic tensile strain on the contractility of HAoSMCs, the changes in cellular morphology, alignment and contractile/synthetic phenotypic markers were assessed under rhythmic low/high strain or static conditions (***Figure 3a***). Cytoskeletal F-actin staining images of HAoSMCs showed a decrease in the cell width and an increase in the cell length in the presence of rhythmic low or high strain (***Figure 3b***). The results also revealed an increase in the length-to-width ratio from 2.33 ± 0.82 under static conditions to 2.74 ± 1.01 under low strain or 3.50 ± 1.19 under high strain (***Figure 3c***). Compared with the irregular orientation of the cells observed under static culture, the cells tended to align perpendicularly to the direction of the applied strain. The angle between the directions of the cellular alignment and the applied strain was approximately 90° (***Figure 3d***). To evaluate the effect of rhythmic tensile strain on the expression of phenotypic markers, the protein levels of SM22, CNN1 and OPN in HAoSMCs were measured by western blotting. The results showed that the contractile phenotype markers SM22 and CNN1 were upregulated under either low or high strain (***Figure 3e-f***). The expression of the synthetic phenotypic marker OPN under both rhythmic low and high strain was lower than that observed under static conditions. These results indicate that the application of rhythmic strain can induce HAoSMCs to spread to longer shapes, align unidirectionally, and exhibit enhanced contractility on the chip model.

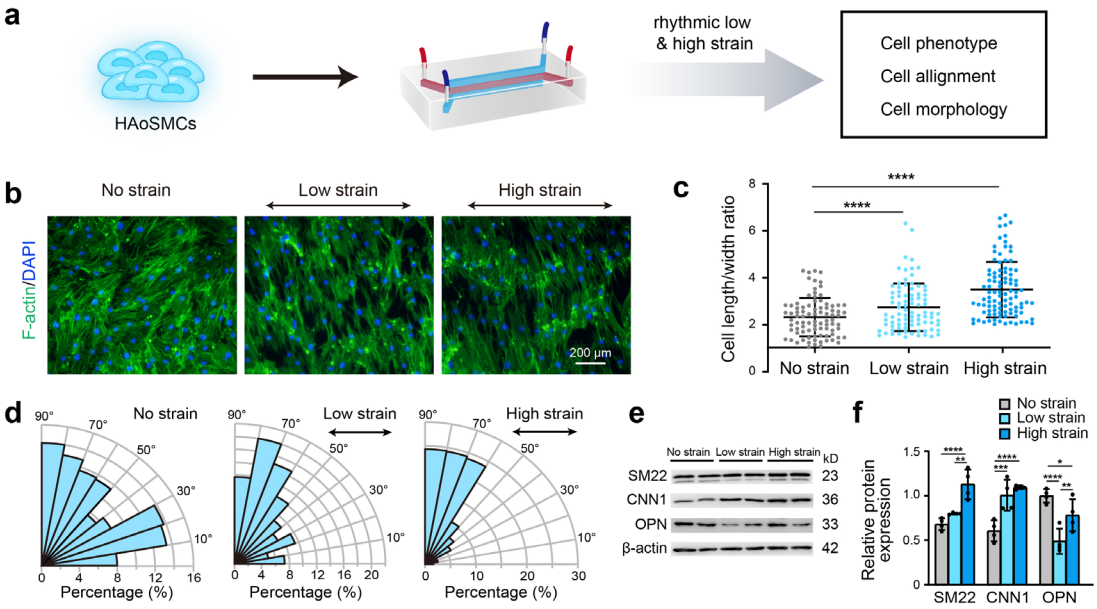

Figure 3. Effect of rhythmic strain on the cell morphology, alignment and phenotype. (**a**) Schematic workflow of cell culture on the chip model. (**b**) Representative images of cytoskeletal F-actin staining of HAoSMCs exposed to low or high rhythmic strain for 24 hrs. The scale bar represents 200 μm. (**c**) Length-to-width ratio of HAoSMCs after exposure to low or high rhythmic strain for 24 hrs. (n = 3, cells were measured in three fields per sample,data from every single cell were plotted. ****P < 0.0001, one-way ANOVA followed by Tukey's post hoc test). (**d**) Alignments of HAoSMCs exposed to low or high rhythmic strain for 24 hrs. (**e**) Representative images of the western blotting analyses of protein markers of the contractile phenotype (SM22 and CNN1) and synthetic phenotype (OPN) of HAoSMCs after exposure to low or high rhythmic strain for 24 hrs. (**f**) Quantification of the total band densities for individual proteins normalized to the corresponding band of β-actin (n = 4, *P < 0.05, **P < 0.01, ***P < 0.001, ****P < 0.0001, one-way ANOVA followed by Tukey's post hoc test). All the data are expressed as the means ± SDs.

The online version of this article includes the following source data for figure 3:
Source data 1. The quantification data for cell length-to-width ratio.
Source data 2. The quantification data for orientation of the cells.
Source data 3. The original raw data for western blotting.

Contractility and mitochondrial dynamics in NOTCH1-insufficient HAoSMCs

To clarify the effect of NOTCH1 insufficiency on HAoSMC contractility, we cultured NOTCH1-insufficient cells under rhythmic low or high strain or static conditions and then characterized the expression of phenotypic markers. The schematic workflow of the experimental design is shown in ***Figure 4a***. First, NOTCH1 was knocked down in HAoSMCs using a lentivirus expressing short hairpin RNA (shRNA) targeting NOTCH1 (***Shao et al., 2015***). To evaluate the effect of the lentivirus vector on NOTCH1 and phenotypic markers, HAoSMCs without any treatments (WT), HAoSMCs treated with negative control shRNA (NC) and HAoSMCs treated with NOTCH1 shRNA (NOTCH1-KD) were verified using quantitative real-time PCR and western blotting experiments. An approximately 60% reduction in NOTCH1 mRNA expression was found in the NOTCH1-KD group compared with the WT and NC groups (***Figure 4—figure supplement 1a***). Under static conditions, the mRNA expression of SM22 and CNN1 was upregulated and that of OPN was downregulated in the NOTCH1-KD group compared with the WT and NC groups (***Figure 4—figure supplement 1a***). The same tendency was found for the protein expression levels by western blotting analysis (***Figure 4—figure supplement 1b-c***).

NOTCH1-KD and WT HAoSMCs were cultured on aorta-on-chip models under rhythmic strain and static conditions to characterize the expression of SM22 and CNN1. As shown in

Figure 4b-c, immunofluorescent staining images showed that SM22 and CNN1 were upregulated in the NOTCH-KD group compared with the WT group under static conditions. However, the opposite results were observed under rhythmic strain conditions: the expression of SM22 and CNN1 in NOTCH-KD HAoSMCs was lower than that in the WT group under rhythmic strain conditions. Western blotting analyses revealed similar alterations in the expression of SM22 and CNN1 (***Figure 4d-e***). In WT HAoSMCs, rhythmic strain induced the upregulation of SM22 and CNN1 expression compared with the levels observed under static conditions. However, a downregulation of SM22 and CNN1 expression was detected in NOTCH-KD HAoSMCs exposed to rhythmic strain. These results suggested that rhythmic strain induced different effects between WT and NOTCH-KD HAoSMCs. In NOTCH-KD HAoSMCs, SM22 and CNN1 expression were higher under static conditions and lower under rhythmic strain than those in WT HAoSMCs.

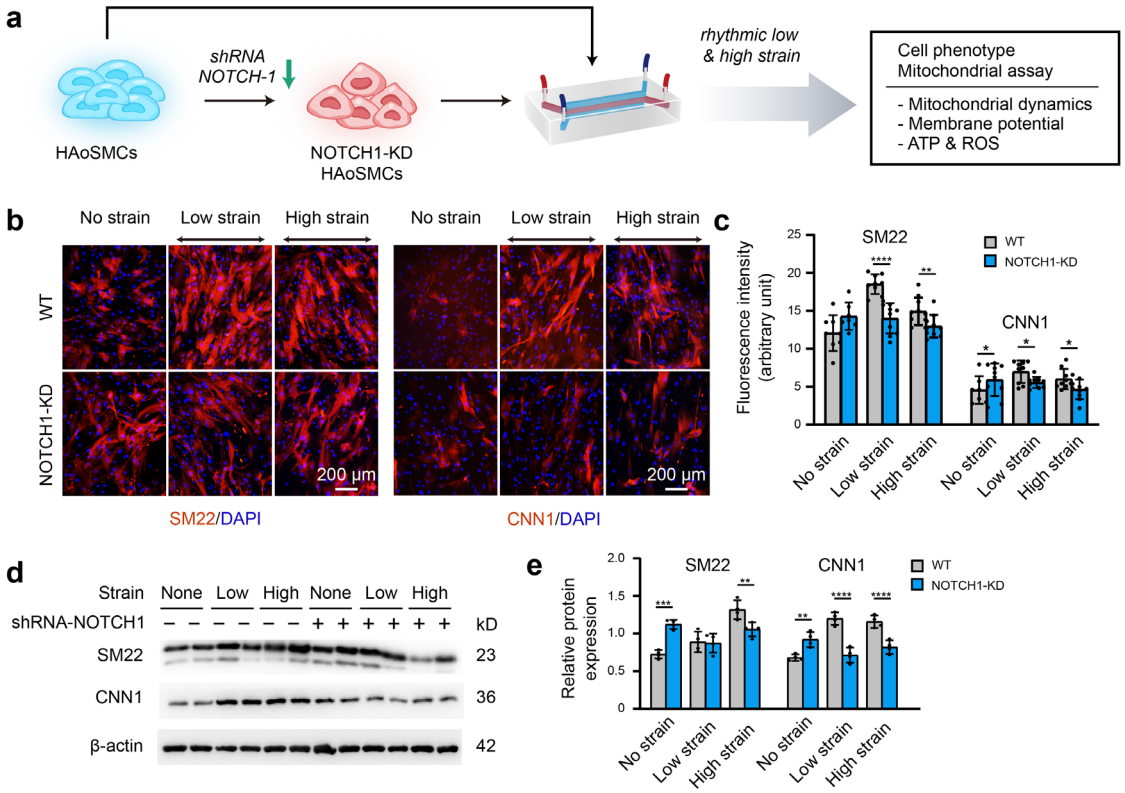

Figure 4. Phenotypic switching of NOTCH1-insufficient HAoSMCs under static and rhythmic strain conditions. (**a**) Schematic workflow of NOTCH1-KD HAoSMCs on the chip model. (**b**) Representative images of immunofluorescence staining of SM22 and CNN1 after exposure to rhythmic low or high strain for 24 hrs. The scale bar represents 200 μm. (**c**) Intensity of immunofluorescence staining of SM22 and CNN1 (n=3, data from three independent biological replicates each with two to four technical replicates were plotted. **P* < 0.05, ***P* < 0.01, *****P* < 0.0001, two-way ANOVA followed by Tukey's post hoc test). (**d**) Representative images of the western blotting analyses of SM22 and CNN1 in the WT and NOTCH1-KD groups exposed to rhythmic low or high strains for 24 hrs. (**e**) Quantification of the total band densities for individual proteins normalized to the corresponding band density of β-actin (n = 4, ***P* < 0.01, ****P* < 0.001, *****P* < 0.0001, two-way ANOVA followed by Tukey's post hoc test). All the data are expressed as the means ± SDs.

The online version of this article includes the following figure supplement(s) and source data for figure 4:

Figure supplement 1. Alteration of NOTCH1 signaling, phenotype and mitochondrial dynamics in HAoSMCs after NOTCH1 shRNA transfection.

Source data 1. The data for intensity of immunofluorescence staining of SM22 and CNN1.

Source data 2. The original raw data for western blotting.

Furthermore, we assessed the alterations in mitochondrial function and dynamics in NOTCH1-KD HAoSMCs. Specifically, western blotting was performed to detect the protein expression of MFN1 and MFN2 (mitochondrial fusion-related proteins) and DRP1 and MFF (mitochondrial fission-related proteins). No significant difference in MFN1, MFN2, DRP1 and MFF protein expression was found between the WT and NC groups under static conditions, which suggested that the expression of these mitochondrial dynamics-related proteins was not affected by the lentivirus vector (***Figure 4—figure supplement 1d-e***). As shown in ***Figure 5a-b***, the expression of MFN1 and MFN2 was downregulated in NOTCH1-KD HAoSMCs under static conditions, and the expression of MFN2 presented a significant difference between the two groups. DRP1 and MFF expression was significantly increased in NOTCH1-KD HAoSMCs under static conditions. Rhythmic strain induced a decrease in MFN1 expression in the NOTCH1-KD group but an increase in the WT group. MFN2 expression was decreased in both the WT and NOTCH1-KD groups after exposure to rhythmic strain but was lower in the NOTCH1-KD group than in the WT group, particularly under rhythmic high strain conditions. Rhythmic strain induced an increase in DRP1 and MFF expression in both the WT and NOTCH1-KD groups, and DRP1 and MFF were highly expressed in NOTCH1-KD HAoSMCs under both rhythmic strain and static conditions (***Figure 5b***). The fragmented mitochondrial morphology observed in NOTHC1-KD HAoSMCs under rhythmic strain conditions indicated decreased mitochondrial fusion, increased mitochondrial fission, i.e., impaired mitochondrial dynamics. As shown in ***Figure 5c***, MitoTracker staining of the mitochondrial shape indicated elongated and interconnected mitochondrial networks in both WT and NOTCH1-KD groups under static conditions. Low or high strain induced alterations of the mitochondrial shape in both WT and NOTHC1-KD HAoSMCs, and these alterations included both a decrease in long rod-shaped elongated interconnected mitochondrial networks and a significant increase in spheroid-shaped fragmented mitochondrial morphology and were more frequent in NOTHC1-KD HAoSMCs under high strain conditions (***Figure 5c-d***).

Mitochondrial dynamics play an important role in the maintenance of normal mitochondrial function. As shown in ***Figure 5e-f***, the fluorescence intensity of the tetramethylrhodamine methyl ester perchlorate (TMRM) staining, which reflects the mitochondrial membrane potential, was lower in NOTHC1-KD HAoSMCs than in the WT group under rhythmic strain. These results indicated loss of mitochondrial membrane potential in NOTCH1-KD HAoSMCs under rhythmic strain. The mitochondrial superoxide (MitoSOX) staining of NOTHC1-KD HAoSMCs was significantly higher than that of the WT group under rhythmic strain (***Figure 5g-h***), which indicated that ROS production was increased in NOTCH1-KD HAoSMCs under rhythmic strain conditions. As an energy source of cells synthesized by mitochondria, the ATP concentration was also evaluated. Rhythmic strain increased the ATP concentration in both WT and NOTHC1-KD HAoSMCs, but under rhythmic strain conditions, a lower ATP concentration was found in NOTCH1-KD HAoSMCs than in WT HAoSMCs (***Figure 5i***). No significant difference in the TMRM or MitoSOX fluorescence intensity or ATP concentration was found between WT and NOTCH1-KD HAoSMCs under static conditions, which indicated that NOTCH1 insufficiency did not affect mitochondrial function under static conditions. Taken together, these data indicated that NOTCH1 insufficiency could induce mitochondrial dysfunction in HAoSMCs by reducing mitochondrial fusion, inducing loss of mitochondrial membrane potential, increasing ROS production and generating insufficient ATP under rhythmic strain, and these effects are accompanied by an impaired contractile phenotype. These findings were consistent with previous studies showing that imbalanced mitochondrial dynamics could induce VSMC dedifferentiation into the synthetic phenotype (***Salabei and Hill, 2013***).

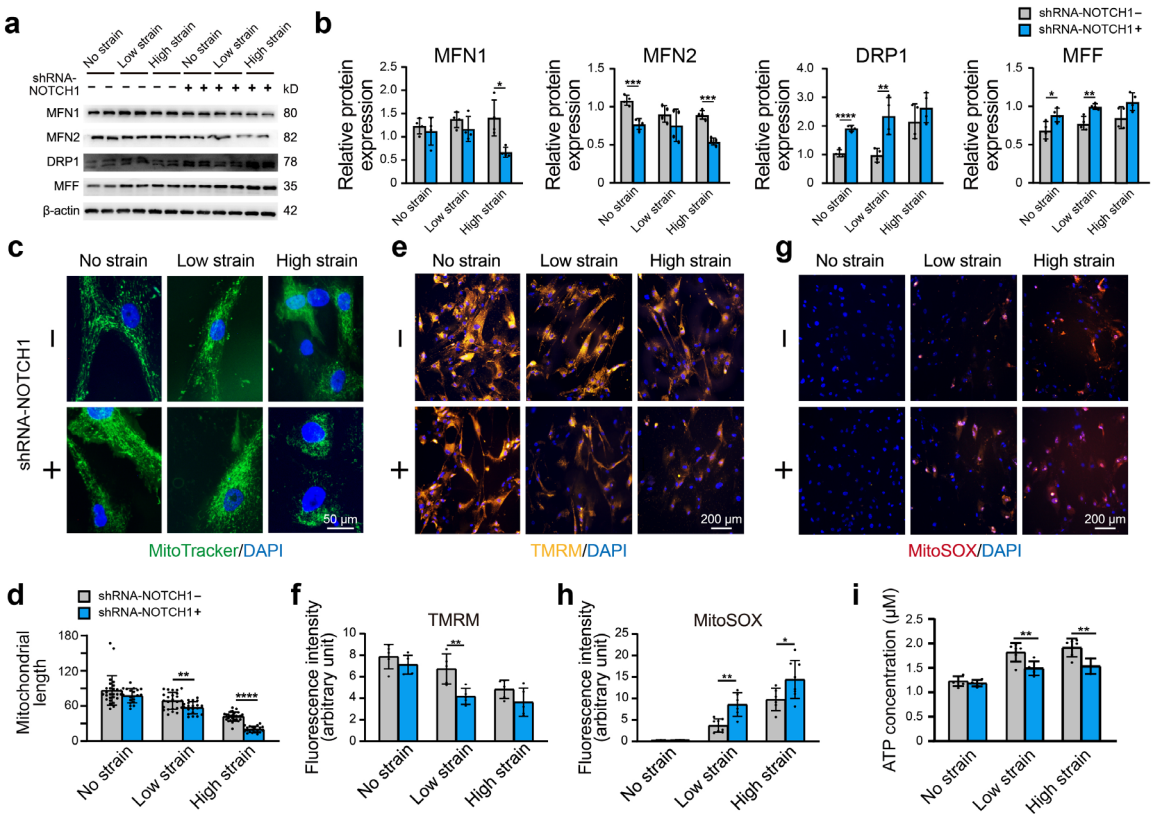

Figure 5. Effect of NOTCH1 insufficiency on mitochondrial dynamics and function in HAoSMCs. (**a**) Representative images of the western blotting analyses of MFN1, MFN2, DRP1 and MFF expression in the WT and NOTCH1-KD groups under rhythmic low or high strain or static conditions. (**b**) Quantification of the total band densities for four individual proteins normalized to the corresponding band density of β-actin (n = 4, **P* < 0.05, ***P* < 0.01, ****P* < 0.001, *****P* < 0.0001, two-way ANOVA followed by Tukey's post hoc test). (**c**) MitoTracker staining images of the mitochondrial morphologies in the WT and NOTCH1-KD groups under rhythmic low or high strain or static conditions. The scale bar represents 50 μm. (**d**) Quantification of the mitochondria length (n = 3, ***P* < 0.01, *****P* < 0.0001, two-way ANOVA followed by Tukey's post hoc test). (**e**) TMRM staining of the mitochondrial membrane potentials in the WT and NOTCH1-KD groups under rhythmic low or high strain or static conditions. The scale bar represents 100 μm. (**f**) Quantification of the relative TMRM fluorescence intensity (***P* < 0.01, two-way ANOVA followed by Tukey's post hoc test). (**g**) MitoSOX staining of mitochondrial superoxide generation in the WT and NOTCH1-KD groups. The scale bar represents 100 μm. (**h**) Quantification of the relative MitoSOX fluorescence intensity (n=3, data from three independent biological replicates each with two to three technical replicates were plotted. **P* < 0.05, ***P* < 0.01, two-way ANOVA followed by Tukey's post hoc test). (**i**) The ATP concentrations were measured using an ATP Determination Kit (n=3, data from three independent biological replicates each with two technical replicates were plotted. ***P* < 0.01, two-way ANOVA followed by Tukey's post hoc test). Quantitative measurements were calculated using ImageJ software. All the data are expressed as the means ± SDs.

The online version of this article includes the following source data for figure 5:

Source data 1. The quantification data for mitochondria length.
Source data 2. The quantification data for relative TMRM fluorescence intensity.
Source data 3. The quantification data for relative MitoSOX fluorescence intensity.
Source data 4. The data for ATP concentrations.
Source data 5. The original raw data for western blotting.

Drugs rescued the impairment of mitochondrial dynamics in NOTCH1-insufficient HAoSMCs from BAV-TAA

To confirm whether the decreased contractile phenotype of NOTCH1-knockdown HAoSMCs can be rescued by inhibition of mitochondrial fission or activation of mitochondrial fusion, we evaluated the phenotypic alterations and mitochondrial dynamics of NOTCH1-insufficient HAoSMCs treated with a mitochondrial fission inhibitor (Mdivi-1) or mitochondrial fusion activators (leflunomide or teriflunomide) under rhythmic high-strain conditions. A schematic workflow of the drug screening experiments was shown in ***Figure 6a***. HAoSMCs purchased from ATCC (CRL1999), primary HAoSMCs (p-HAoSMCs) isolated from patients in the non-diseased group and p-HAoSMCs purchased from ATCC (PCS-100-012) were transfected with NOTCH1-shRNA to generate NOTCH1-knockdown HAoSMCs.

The effect of drug testing on aorta-on-a-chip model was desirable, even though the results did not exhibit all the positive responses. In the CRL1999 HAoSMCs (***Figure 6b***), all three drugs enhanced MFN1 and MFN2 expression to different extents, and the greatest increase in MFN1 expression was obtained with Mdivi-1. In addition, the three drugs all decreased DRP1 expression to different extents but did not affect MFF expression. The three drugs also increased SM22 and CNN1 expression to different extents, and the maximal expression of SM22 and CNN1 was obtained with leflunomide. In p-HAoSMCs isolated from patients in the non-diseased group (***Figure 6c***), the three drugs increased MFN1 expression, but no significant difference was found compared with the control group. Teriflunomide significantly increased MFN2 and DRP1 expression and significantly decreased MFF expression. Although the effects of these drugs on mitochondrial dynamics were not desirable, all three drugs increased the expression of SM22 and CNN1 to different extents. In PCS-100-012 p-HAoSMCs (***Figure 6d***), none of the three drugs exerted an obvious effect on MFN1, MFN2 and DRP1 expression, and teriflunomide significantly decreased MFF expression. All three drugs increased the expression of SM22 and CNN1 to different extents.

To further evaluate the potential of these drugs for clinical use in the treatment of NOTCH1-insufficient patients with BAV-TAA, we isolated p-HAoSMCs from the aortic tissues of three individual patients with BAV-TAA. The clinical characteristics of three patients with BAV-TAA are shown in ***Supplementary File-Table V***. Significantly lower NOTCH1 protein expression was found in p-HAoSMCs from BAV-TAA aortic tissues compared with p-HAoSMCs from non-diseased aortic tissue (***Figure 6—figure supplement 1***). A significant reduction in MFN1 and MFN2 expression was found in p-HAoSMCs from BAV-TAA aortic tissues under static and rhythmic high-strain conditions. We also found that SM22 and CNN1 expression was significantly reduced in p-HAoSMCs from BAV-TAA aortic tissues under rhythmic high-strain conditions (***Figure 6—figure supplement 1***). The three drugs exerted different effects on mitochondrial dynamics-related proteins (***Figure 6e-g***). All three drugs enhanced MFN2 expression to different extents, and maximal MFN2 expression was obtained with the treatment of teriflunomide. The three drugs increased MFN1 expression and decreased DRP1 expression to different extents in two lines of BAV-TAA p-HAoSMCs, and the greatest decrease in DRP1 expression was obtained with teriflunomide. The three drugs decreased MFF expression to different extents in the two lines of BAV-TAA p-HAoSMCs and exerted different effects on the expression of the contractile proteins SM22 and CNN1, and teriflunomide significantly increased SM22 expression in the two lines of BAV-TAA p-HAoSMCs. All three drugs enhanced CNN1 expression to different extents, and Mdivi-1 or teriflunomide significantly increased CNN1 expression in one line of BAV-TAA p-HAoSMCs. The data from BAV-TAA p-HAoSMCs indicated that teriflunomide exerted a more obvious effect on rescuing impaired mitochondrial dynamics and the expression of the contractile phenotype proteins SM22 and CNN1 under rhythmic high-strain conditions. These results indicated that leflunomide, Mdivi-1, and, in particular, teriflunomide, could serve as drug candidates for ameliorating the disease progression of BAV-TAA.

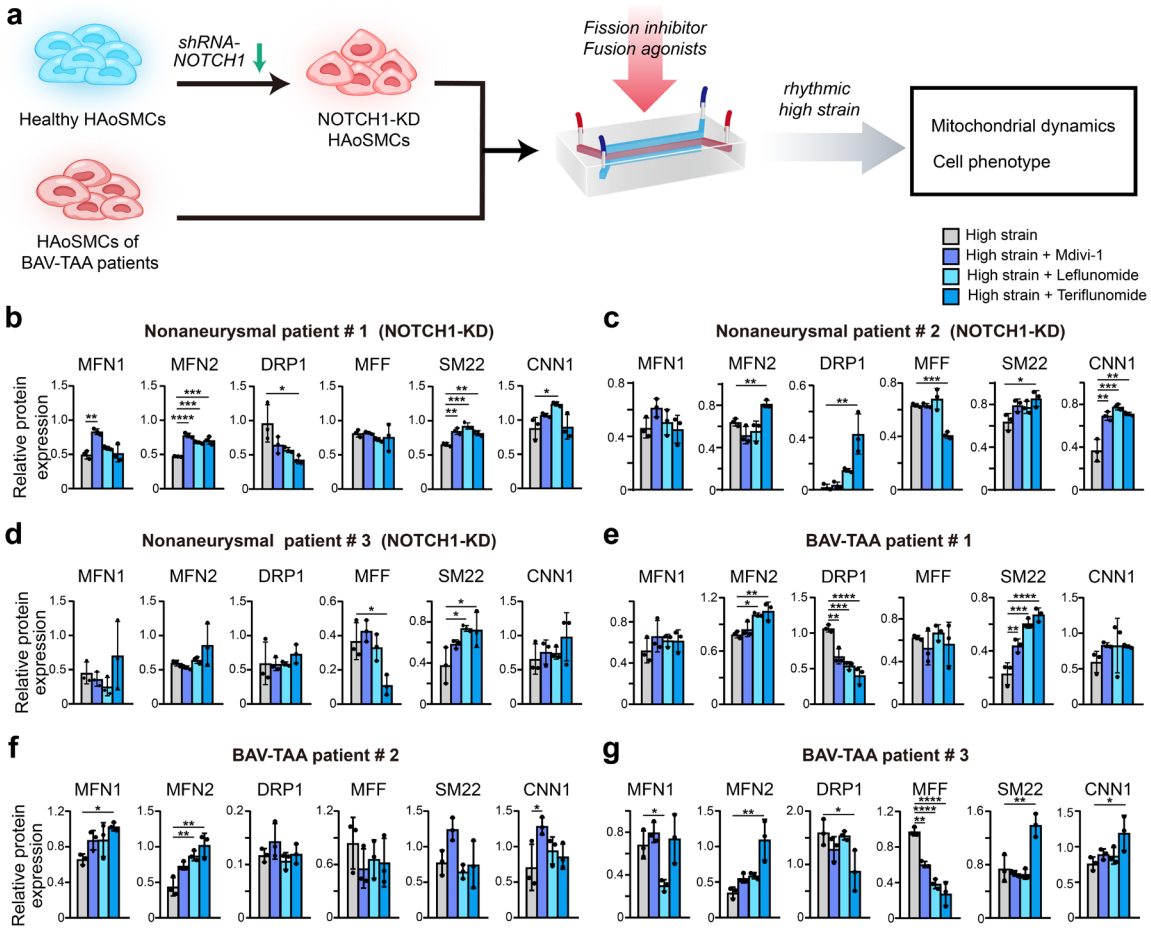

Figure 6. Screening of drugs that can rescue the cell phenotype and mitochondrial dynamics using the chip model. (**a**) Schematic workflow of the experimental design. After treatment with treated with Mdivi-1, leflunomide and teriflunomide on the chip models with (**b**) a NOTCH1-knockdown HAoSMC cell line (CRL1999), (**c**) NOTCH1-knockdown p-HAoSMCs isolated from non-diseased aortic tissues, (**d**) NOTCH1-knockdown p-HAoSMCs purchased from ATCC, and **(e-g)** p-HAoSMCs isolated from aortic tissues from three patients with BAV-TAA, quantification of the total band densities of the mitochondria-related proteins MFN1, MFN2, DRP-1, and MFF and the contractile phenotype proteins SM22 and CNN1 were normalized to the corresponding band densities of β-actin. All the data are expressed as the means ± SDs. n = 3, **P* < 0.05, ***P* < 0.01, ****P* < 0.001, *****P* < 0.0001, one-way ANOVA followed by Tukey's post hoc test.

The online version of this article includes the following figure supplement(s) and source data for figure 6:
Figure supplement 1. Expression NOTCH1, phenotype and mitochondrial dynamics related proteins in p-HAoSMCs from BAV-TAA aortic tissues.
Source data 1. The original raw data for western blotting.

Discussion

In this study, protein analyses of human aortic aneurysm tissues suggested the insufficient expression of NOTCH1 in BAV-TAA was associated with the impaired mitochondrial dynamics and OXPHOS. To verify it, we established a microfluidic aorta-on-a-chip model that enabled us to reproducibly generate the rhythmic tensile strain of the native human aortic wall. We showed that this model could apply a biomimetic rhythmic tensile strain with a confined amplitude/magnitude and rhythm to HAoSMCs. We also confirmed that impaired mitochondrial fusion contributed to the

attenuated contractile phenotype observed in NOTCH1-KD HAoSMCs. We further identified that MFN1/2 agonists and DRP1 inhibitors were able to reverse the imbalance in mitochondrial dynamics and partly rescue the contractile phenotype in NOTCH1-insufficient HAoSMCs.

The majority of studies on the molecular mechanism and pharmacotherapy for TAA have been conducted using conventional cell culture models and animal models. The pathophysiological features of human aortic aneurysm can be induced in animal models by elastase, calcium chloride, angiotensin II or transgenesis, which partially enable investigation of the etiology, pathogenesis, and therapeutic targets of TAA at an early stage (***Eckhouse et al., 2013; Ikonomidis et al., 2003; Mao et al., 2015***). However, all these animal models cannot replicate the native characteristics of BAV-TAA. Moreover, the apparent species gap between preclinical animal experiments and clinical studies might also impede pharmaceutical discovery (***Lindeman and Matsumura, 2019***). In contrast, the shortcoming of the conventional cell culture model of aortic disease lies in its inability to recapitulate *in vivo* biomechanical stimuli. Advances in microfabrication and microfluidics have provided novel techniques for building organ-on-a-chip models that integrate rhythmic tensile strains into *in vitro* cell culture. Organ-on-a-chip models can be broadly defined as any form of microfabricated cell culture device that models organ-specific biochemical and physical microenvironments (***Zhao et al., 2019; Park et al., 2019***) and represent an *in vitro* platform that is complementary to animal models. By anatomizing the complexity of the biomechanical microenvironment, this study focused on the physiological rhythmic strain on HAoSMCs in the aortic tunica media, which plays a central role in the pathogenesis of aneurysms. In particular, the strain of the ascending aorta, which was defined as the maximal change in the ascending aorta diameter over a cardiac cycle, can vary diversely from a low value of 7.0 ± 2.5% to a high value of 21.5 ± 12.4% depending on age, sex and disease severity (***Akazawa et al., 2016; Bell et al., 2014; Morrison et al., 2009***). Under rhythmic strain, healthy HAoSMCs maintain a contractile phenotype, which allows regulation of the vascular tone. While, diseased HAoSMCs dedifferentiate into a synthetic phenotype under pathological conditions, and this dedifferentiation represents the initial step toward an aneurysm pathology (***Petsophonsakul et al., 2019***). The aorta-on-a-chip model developed in this study featured the controlled magnitude and rhythm of mechanical stimuli relevant to the human pathophysiological parameters of aorta biomechanics.

NOTCH1 has an important role in the maintenance of normal mitochondrial dynamics. Previous studies have reported that the expression of NOTCH1 signaling was attenuated in the aortic tissues of patients with BAVs (***Sciacca et al., 2013***). Additionally, Balistreri et al. found decreased mRNA levels of NOTCH1-4 in aortic aneurysm tissues and decreased protein levels of soluble NOTCH1 in plasma (***Balistreri et al., 2018***). Using clinical samples, our protein analysis also indicated that patients with BAV-TAA presented lower expression of NOTCH1 protein in ascending aortic aneurysms; and the NOTCH1 insufficiency was accompanied with attenuated mitochondrial fusion. This was consistent with the previous studies that reported NOTCH1 regulates mitochondria dynamics in cardiovascular cell differentiation and survival. Kasahara et al. found that mitochondrial fusion regulates the differentiation of myocardial cells through NOTCH1 signaling pathway (***Kasahara et al., 2013***). Here, we found that NOTCH1 insufficiency induced mitochondrial dysfunction in HAoSMCs by reducing mitochondrial fusion, along with loss of mitochondrial membrane potential, increasing ROS production and generating insufficient ATP under rhythmic strain. These results indicated that the relationship between impaired mitochondrial fusion and NOTCH1 deficiency in BAV-TAA. Consistently, we found decreased contractile phenotype in NOTCH1-deficient HAoSMCs under rhythmic tensile strain and in BAV-TAA aortic tissues, accompanied by lower NOTCH1 expression and impaired mitochondrial fusion.

NOTCH1 signaling is also involved in the regulation of HAoSMCs differentiation and the expression of contractile proteins. HAoSMCs are highly plastic cells and undergo reversible changes in phenotype in response to environmental stimuli (***Vasquez-Trincado et al., 2016***). Differentiated HAoSMCs have a contractile phenotype with little proliferation and little secretion of extracellular matrix. HAoSMCs transform from a contractile into a synthetic phenotype and induce

loose of vascular tone, which is one of the major pathological process in TAA. In this study, we found that NOTCH1 insufficiency in HAoSMCs downregulated the contractile phenotype proteins SM22 and CNN1 under rhythmic strain. Also, the expressions of SM22 and CNN1 were decreased in BAV-TAA aortic tissues compared to non-diseased aortic tissues. Noseda et al. reported that NOTCH1 activation was needed for expression of the contractile phenotype protein αSMA in VSMCs *via* the NOTCH/CSL axis (***Noseda et al., 2006***). High et al. reported that NOTCH1 promotes the differentiation of the cardiac neural crest into differentiated VSMCs and the expression of αSMA (***High et al., 2007***). However, the specific mechanism by which NOTCH1 leads to a reduced contractile phenotype has not been fully investigated. Based on results obtained from the aorta-on-a-chip model, it comes to the assumption that NOTCH1-insufficiency reduced the contractile phenotype through decreasing mitochondrial fusion.

Mitochondrial dynamics itself has been recognized as one of the critical factors that regulate the phenotype switching of vascular smooth muscle cells (VSMCs). Salabei and Hill reported that PDGF-BB induces the dedifferentiation of VSMCs into the synthetic phenotype through overactivation of mitochondrial fission (***Salabei and Hill, 2013***). Chen et al. found that the expression of MFN2 is markedly reduced in hyperproliferative VSMCs from spontaneously hypertensive rat arteries (***Chen et al., 2004***). Using the aorta-on-a-chip model, we demonstrated the decreased mitochondrial fusion in NOTCH1-insufficient HAoSMCs, accompanied with decreased contractile phenotypes. Thus, mitochondrial dynamics regulated by NOTCH1 may have a role in maintains of contractile phenotype. In addition, we also found the contractile phenotype was upregulated in NOTCH1-insufficient HAoSMCs after treatment with mitochondrial fusion activators and mitochondrial fission inhibitors, which further verified the hypothesis that contractile phenotype of HAoSMCs was regulated by NOTCH1-mitochondrial fusion axis. In clinical samples, our protein analysis indicated that aortic tissues from patients with BAV-TAA presented the reduced expressions of mitochondrial fusion proteins and contractile phenotype proteins, compared with non-diseased aortic tissues. Further, the mass spectrometry-based proteomic analysis of aortic tissue samples indicated that mitochondrial dysfunction and OXPHOS pathways were significantly altered in BAV-TAA aortic tissues. Consistent with the previous single-cell transcriptome analysis, TAA aortic tissues showed decreased mitochondrial function; and this finding suggests that OXPHOS ATP production might be insufficient for VSMC contractile activities (***Li et al., 2020***). Therefore, maintaining normal mitochondrial dynamics *via* NOTCH1 could be one of the mechanisms through which NOTCH1 regulates HAoSMCs's contractility and maintains vascular wall tension. However, the specific mechanism by which reduced mitochondrial fusion causes a reduction in the contractile phenotype requires further investigation. In addition, our proteomic analysis of tissue samples showed that several mitochondrial dysfunction-related pathways, namely, EIF2 signaling and the sirtuin signaling pathway, were also altered in BAV-TAA aortic tissue, which may provide research directions to investigate further mechanisms.

Lastly, we demonstrated that MFN1/2 agonists and DRP1 inhibitors reversed the imbalanced mitochondrial dynamics in BAV-TAA p-HAoSMCs with intrinsic NOTCH1 insufficiency or in NOTCH1-KD HAoSMCs on the aorta-on-a-chip model, which provides a prototype for an *in vitro* drug testing platform. Two FDA-approved drugs, leflunomide or teriflunomide, rescued the contractile phenotype of BAV-TAA p-HAoSMCs and showed their potential to ameliorate disease progression. Zorzano's group first found that dihydroorotate dehydrogenase inhibitors (leflunomide, teriflunomide, or brequinar sodium) could promote mitochondrial elongation through induction of the mitochondrial proteins MFN1 and MFN2 in HeLa cells (***Miret-Casals et al., 2018***). The experimental data obtained in this study encourage further studies on the application of leflunomide and teriflunomide in BAV-TAA.

In conclusion, we constructed a aorta-on-a-chip model, which could serve as a complementary tool to the current cell culture system and animal models. Using the aorta-on-a-chip model, we found that NOTCH1 insufficiency in HAoSMCs induced phenotypic switching from a contractile to a synthetic phenotype accompanied by an impairment of mitochondrial fusion, implying its potential role as a therapeutic target for BAV-TAA. At the current stage, *in vitro*

532 microphysiological models and animal models are complementary to each other in the sense that
533 they are able to provide more comprehensive basis for preclinical assays with greater predictive
534 power.

535 **Materials and Methods**

536 **Aorta-on-a-chip model design and fabrication**

537 The structure of the three-layer microfluidic aorta-on-a-chip model was designed using computer-
538 aided design (CAD) software (Autodesk Inc). The size of the three layers were 100 mm × 40 mm
539 × 6 mm. The top and bottom layers had microchannels with dimensions of 70 mm × 6 mm × 4
540 mm, and the middle layer contained a microchannel with dimensions of 70 mm × 6 mm × 6 mm.
541 Molds of the three layers were custom-made using a high-precision computer numerical control
542 (CNC) engraving machine (Jingyan Technology). The frame of the molds and the microchannels
543 were carved out of polymethyl methacrylate (PMMA) plates, which were then glued on another
544 PMMA plate. Polydimethylsiloxane (PDMS, Sylgard 184, Dow Corning) was polymerized in
545 defined casts at a weight ratio of base to curing agent of 10:1. The mixed PDMS was poured into
546 the molds and underwent cross-linking at 70°C for 2 hrs. Commercialized PDMS membranes
547 were purchased from Hangzhou Bald Advanced Materials (thickness, 200 ± 2 μm; Young's
548 modulus, 1.7 MPa). Subsequently, the three PDMS layers were peeled off the molds. The bottom
549 layer of the PDMS slab was bonded with one PDMS membrane after oxygen plasma treatment
550 (Harrick Plasma), and the top PDMS layer was bonded to another PDMS membrane in a similar
551 manner. The middle PDMS layer was then sandwiched between the top and bottom membranes;
552 this step was performed under a microscope to guarantee that the upper and lower
553 microchannels fully overlapped with the middle microchannel.

554 **Mechanical stimulation**

555 The cells were stretched by applying different percentages of rhythmic strain to the PDMS
556 membranes for 24 hrs. The vacuum pump was connected to a water-oil separator, which dried
557 the gas to protect the downstream vacuum regulator and solenoid valve. The inlet of the vacuum
558 pumps was then connected to the computer-controlled solenoid system by applying rhythmic
559 stretching at a frequency of 1 Hz and then connected to the gas channel of the aorta-on-a-chip
560 model. The regulator was used to control the vacuum magnitude. The solenoid valve was a
561 voltage-dependent on/off valve used to control the stretching frequency of the PDMS membrane.
562 When the supply voltage was greater than 24 V, the gas in the channel was pumped out, which
563 stretched the PDMS membrane. Otherwise, the gas channel was connected to the atmosphere,
564 and the membrane deformation recovered. The on/off frequency of the solenoid valve was
565 controlled by a microcontroller unit (MCU). Thus, the stretching frequency could be controlled by
566 changing the preset program of the MCU, and the stretching amplitude could be controlled by
567 adjusting the vacuum regulator manually. We used two pressure ranges, 10 kPa (7.18 ± 0.44%,
568 low strain) and 15 kPa (17.28 ± 0.91%, high strain), throughout the experiments. As the control,
569 cells were cultured in aorta-on-a-chip models under static conditions. After 24 hrs of rhythmic
570 strain, samples were collected for immunofluorescence, RT-qPCR, western blotting and
571 mitochondrial membrane dynamics analyses.

572 **Human aortic sample collection**

573 Written informed consent was obtained from all patients before participation. Human aortic
574 specimens were utilized under approvals of Zhongshan Hospital, Fudan University Ethics
575 Committee (NO. B2020-158) in accordance with the Declaration of Helsinki. Human aortic
576 samples were collected from patients who underwent ascending aorta surgery at Zhongshan
577 Hospital, Fudan University. Echocardiography was used to characterize aortic valve morphology
578 and ascending aortic diameter prior to surgery. The tissue samples were immediately frozen in
579 liquid nitrogen and stored at -80°C. Six aortic tissues were obtained from patients with a tricuspid
580 aortic valve but without aortic dilation (non-diseased; mean age: 37.7 years; range: 22-47 years;
581 4 males), and another six samples were obtained from patients with BAV-related thoracic aortic

aneurysm (BAV-TAA; mean age: 59.3 years; range: 43-72 years; 4 males). The patients' basic information is available in ***Supplementary File-Table I***.

Primary human smooth muscle cell isolation

Primary human aortic smooth muscle cells (p-HAoSMCs) were isolated from non-diseased aortic tissues and BAV-TAA aortic tissues (n = 3). The aortic tissues were washed with phosphate-buffered saline (PBS, Thermo Fisher Scientific). The intima and adventitia layers of the tissues were removed, and the media layer was preserved for the harvesting of p-HASMCs. Subsequently, the media layer was cut into small pieces (2-3 mm in length) and cultured in high-glucose Dulbecco's modified Eagle's medium (DMEM, Gibco) with 20% fetal bovine serum (FBS, Gibco) and 1% penicillin and streptomycin (p/s, Gibco) for 2-3 weeks at 37°C and 5% CO_2 in a humidified incubator. After approximately 10-12 days, the p-HASMCs started to migrate out of the tissue pieces. When the cells reached approximately 80% confluency, first-passaged cells were rinsed with PBS, digested using 0.25% trypsin (Gibco), and replated in smooth muscle cell culture medium (SMCM, ScienCell). The cells were characterized through an immunofluorescence analysis of four different specific markers of smooth muscle cells (CNN1, SM22, MYH11 and α-SMA). We used p-HASMCs at a low passage (P2-P5) in all the experiments.

Cell culture

In addition to the p-HAoSMCs isolated from aortic tissues, a human aortic smooth muscle cell line (CRL1999) and commercialized p-HAoSMCs (PCS-100-012) were purchased from ATCC in accordance with their ethical regulations and compliances. p-HAoSMCs and the CRL1999 cell line were cultured in SMCM. Prior to cell seeding, the surface of the cell culture channel was coated with mouse collagen at a concentration of 80 μg/mL (Sigma) by incubating for 1 hr at room temperature and drying for 2 hrs at 70°C. Afterward, the cell culture channel was washed with PBS, and cells were seeded on the PDMS membranes in a cell culture channel at a density of 2 x 10^6 cells/mL. The cells were cultured in Dulbecco's modified Eagle's medium/nutrient mixture F-12 (DMEM/F-12, Thermo Fisher Scientific) supplemented with 10% FBS in a cell culture channel. After seeding, aorta-on-a-chip models were incubated at 37°C and 5% CO_2 in a humidified incubator for 24 hrs for cell attachment. The aorta-on-a-chip models were then ready for mechanical stimulation experiments.

Drug screening

Mdivi-1 (Sigma), an inhibitor of mitochondrial fission, was dissolved in dimethylsulfoxide (DMSO) and stored at -20°C before use, and fresh medium was used to obtain a final concentration of 30 μM. Leflunomide and teriflunomide (Sigma), two different activators of mitochondrial fusion, were dissolved in DMSO at appropriate concentrations. Prior to cell treatment, fresh medium was used to obtain a concentration of 75 μM for both drugs. After the cells were fully attached to the PDMS membrane in the cell culture channel, medium containing a mitochondrial fusion activator (leflunomide and teriflunomide) or mitochondrial fission inhibitor (Mdivi-1) was added to the aorta-on-a-chip models. After 24 hrs of rhythmic strain, the samples were collected for comparative experiments.

Immunofluorescence analysis

Immunofluorescence analysis was performed in the microfluidic aorta-on-a-chip model *in situ* after 24 hrs of rhythmic stretch. The medium was aspirated from the cell culture channel, and the cells were washed with PBS, immediately fixed with 4% paraformaldehyde (Beyotime) for 30 min at room temperature and permeabilized with 1% (v/v) Triton X-100 (Beyotime) for 15 min. Afterward, blocking solution with 5% bovine serum albumin (Sigma) was applied to the cells to block nonspecific binding sites for 30 min at room temperature, and the cells were incubated overnight at 4°C with primary antibodies. The primary antibodies used in this study and their working concentrations are listed in ***Supplementary File-Table VI***. After incubation, the cells were washed three times with PBS and incubated with Alexa 594 anti-rabbit secondary antibody (Thermo Fisher Scientific) at a dilution of 1:300 for 1 hr at room temperature under dark

conditions. The nuclei were counterstained with 4′,6-diamidino-2-phenyllindole (DAPI) (Thermo Fisher Scientific) for 10 min. The aorta-on-a-chip models were then disassembled, and images were acquired with a fluorescence microscope (Leica DMi8) and analyzed using ImageJ software.

Western blotting

Cells and aortic tissue samples were lysed using RIPA (Beyotime) lysis buffer supplemented with protease inhibitor phenyl methyl sulfonyl fluoride (PMSF, Beyotime). To collect an appropriate concentration of protein for western blotting, we collected and pooled cell protein from three microfluidic aorta-on-a-chip model. For the tissue samples, the intima and adventitia were peeled out, and the middle layers were ground into small pieces. The extracts were incubated for 30 min on ice for complete lysis and centrifuged at 14,000 rpm and 4°C for 25 min. The supernatant was collected after centrifugation, and the debris was discarded. The protein concentrations were quantified using a BCA Protein Assay kit (Thermo Fisher Scientific). The extracted proteins were diluted in sample loading buffer and heated for 5 min at 95°C. Ten micrograms of each protein sample was then separated by running on a 10% SDS-PAGE gel and subsequently transferred to 0.2-μm polyvinylidene fluoride (PVDF) membranes (Millipore). The PVDF membranes were blocked with 5% skimmed milk (Beyotime) for 1 hr at room temperature and incubated with different primary antibodies (***Supplementary File-Table VI***) overnight at 4°C. The membranes were then incubated with horseradish peroxidase-conjugated goat anti-rabbit and goat anti-mouse IgG secondary antibodies (Cell Signaling Technology) at 1:6000 dilution for 1 hr at room temperature. Bands were detected using the SuperSignal chemiluminescence reagent substrate (Millipore). The protein expression level was normalized using the housekeeping protein β-actin. Quantitative estimation of the band intensity was performed using Image J software.

Knockdown of NOTCH1 by lentivirus short hairpin RNA

NOTCH 1-targeted short hairpin RNA (shRNA) was designed and synthesized by GeneChem. p-HASMCs and CRL-1999 cells were seeded in six-well plates (6 x 10^5 cells/well) and cultured in a humidified incubator at 37°C with 5% CO_2. When the cells reached 30% confluency, the cells were divided into three groups: control (WT), negative control shRNA (NC) and NOTCH1 knockdown (NOTCH1-KD). The cells in the NC and NOTCH1-KD groups were infected with lentivirus-nonspecific shRNA and lentivirus-shRNA-NOTCH1 at a multiplicity of infection (MOI) of 10 according to the manufacturer's recommended protocol (GeneChem). After 8-12 hrs of infection, the virus particles were removed from the respective wells, and fresh SMCM was added. The cells were further cultured for 72 hrs in a humidified incubator at 37°C with 5% CO_2. To establish a stable cell line, the cells were treated with puromycin at a concentration of 2 μg/mL for 5 days. When the cells reached approximately 80% confluency, the cells were harvested, and the knockdown efficiency of NOTCH1 was evaluated by qRT-PCR and western blotting assays.

Morphology and membrane potential analyses of mitochondria

For analyses of the mitochondrial morphology and membrane potential, we used different types of fluorescent dyes, including tetramethylrhodamine methyl ester (TMRM), MitoSOX, and MitoTracker (all from Thermo Fisher Scientific), according to the manufacturer's guidelines. Cells were stretched on aorta-on-a-chip models for 24 hrs. An appropriate concentration of each fluorescent dye was added to three different aorta-on-a-chip models and incubated at 37°C for 30 min in the dark. After incubation, the channels were washed three times with PBS, and the nuclei were counterstained with Hoechst (Sigma) for 10 min. Representative staining images of all three fluorescent dyes (under static and strain conditions) were acquired using a fluorescence microscope (Leica) and analyzed using Image J software.

Estimation of the ATP concentration

The level of ATP production by cells on the aorta-on-a-chip models was determined using an ATP assay kit (Beyotime) following the manufacturer's instructions. In brief, after mechanical stimulation of the cells on the aorta-on-a-chip models, the cells were lysed using ATP lysis buffer, and total protein was collected by centrifugation of the cell lysate at 12000 rpm and 4°C for 5 min.

After centrifugation, the supernatant was collected, mixed with ATP detection reagent and incubated for 10 min at room temperature. After incubation, the ATP concentration was measured using a luminometer. An ATP concentration standard curve was then established and used to calculate the ATP concentration of each sample.

Mass spectrometry analysis

The aortic samples were minced and lysed with RIPA on ice for 30 min. The extracts were centrifuged at 14,000 rpm and 4°C for 25 min, and the supernatant was collected after centrifugation. The protein concentrations were quantified using a BCA Protein Assay kit (Thermo Fisher Scientific). Filter-aided sample preparation (FASP) was performed for protein digestion. Before alkylation with 10 mM dithiothreitol (DTT, Sigma) and 30 mM iodoacetamide (IAA, Sigma), the proteins were loaded in 10-kDa centrifugal filter tubes (Millipore) and treated twice with 50 mM NH_4HCO_3 (Sigma). The extracts were digested with trypsin at a ratio of 1:50 and incubated at 37°C overnight. Trifluoroacetic acid (TFA, 0.1%) was added to stop the digestion reaction. One hundred micrograms of peptides containing 0.1% TFA was loaded in high-pH reversed-phase fractionation spin columns (Thermo Fisher Scientific). We obtained 10 flow-through fractions, and two fractions were combined to obtain one sample. The resulting five fractions were dried by vacuum centrifugation. The samples were resuspended in 30 µL of solvent A (A: water with 0.1% formic acid; B: ACN with 0.1% formic acid), separated by nanoLC and analyzed by on-line electrospray tandem mass spectrometry. The experiments were performed using a nanoAquity UPLC system (Waters Corporation) connected to a quadrupole-Orbitrap mass spectrometer (Q Exactive HF) (Thermo Fisher Scientific) equipped with an online nanoelectrospray ion source. Two microliters of peptide sample was loaded onto an analytical column (Acclaim PepMap C18, 75 µm x 25 cm) and subsequently separated with a linear gradient from 5% B to 30% B over 110 min. The column flow rate was maintained at 300 nL/min, and the column temperature was maintained at 45°C. An electrospray voltage of 2.2 kV versus the inlet of the mass spectrometer was used.

The Q Exactive HF mass spectrometer was operated in the data-dependent mode to switch automatically between MS and MS/MS acquisition. Survey full-scan MS spectra (m/z 350-1500) were acquired with a mass resolution of 60 K. The automatic gain control (AGC) was set to 3000000 with a maximum injection time of 50 ms. Fifteen sequential high-energy collisional dissociation (HCD) MS/MS scans with a resolution of 15.0 K were acquired with the Orbitrap. The intensity threshold was 50000, and the maximum injection time was 80 ms. The AGC target was set to 100000, and the isolation window was 1.6 m/z. Ions with charge states of 2+, 3+ and 4+ were fragmented with a normalized collision energy (NCE) of 30%. In all cases, one microscan was recorded using dynamic exclusion of 20 s. In the MS/MS, the fixed first mass was set to 110. Online peaks were used for the analysis of proteomic data. The precursor mass error tolerance was set to 10 ppm with a fragment mass error tolerance of 0.05 Da. In all software programs, carbamidomethylation was set as a fixed modification, and variable modifications of oxidation (M), acetylation (N-term) and deamidation (NQ) were included. The false discovery rate (FDR) for peptide and protein identifications was set to 1%. Total ion chromatography (TIC) was used for normalization. The rest of the parameters were set to the default values. The MS/MS spectra were searched using the Andromeda search engine against the Swiss-Prot database (Taxonomy: Homo sapiens, Release 2020-11-02) (total of 20385 entries). The statistical analyses were mainly conducted in R 3.6.1. Label-free quantification (LFQ) was used for the following analysis flow. Proteins containing more than 50% missing values were removed, and the remaining missing values were inputted by k-nearest neighbor (kNN) imputation based on the Euclidean distance using the DMwR package in R. After normalizing the trimmed mean of M-values (TMM), PCA showed no significant batch effect. Differential expression analysis was conducted using the Limma package. The proteins with a p-value threshold of 0.05 and fold change > 1.5 were identified as differentially expressed proteins and inputted into the IPA. The mass spectrometry proteomics data have been deposited to the ProteomeXchange Consortium via the PRIDE partner repository with the dataset identifier PXD026303.

Statistical analyses

The experimental results are expressed as the means ± standard deviations (SDs). A minimum of three individual replications of each group were used for the relative analyses. The statistical analyses were performed using GraphPad Prism 8 software. Two-tailed Student's t tests were used to compare values between two groups, and one-way or two-way analysis of variance (ANOVA) followed by Tukey's post hoc test was used for multiple-group comparisons. Statistical significance was indicated by *$P < 0.05$*, **$P < 0.01$*, ***$P < 0.001$* and ****$P < 0.0001$*.

Acknowledgments

We Thank Drs. Fei Lan, Faxing Yu, Dan Ye, and Jiandong Ding at Fudan University for the helpful scientific discussions.

Author Contributions

Mieradilijiang Abudupataer, Conceptualization, Formal analysis, Investigation, Visualization, Methodology, Resources, Data curation, Validation, Methodology, Writing -original draft, Writing - review and editing; Shichao Zhu, Formal analysis, Validation, Investigation, Methodology; Shiqiang Yan, Software, Formal analysis, Methodology, Visualization; Kehua Xu, Software, Formal analysis, Methodology; Jingjing Zhang, Formal analysis, Validation, Investigation; Shaman Luo, Investigation, Methodology; Wenrui Ma, Resources, Formal analysis, Investigation; Md. Fazle Alam, Writing - review and editing; Yuyi Tang, Investigation, Methodology; Hui Huang, Investigation, Formal analysis; Nan Chen, Resources; Li Wang, Validation, Writing - review and editing; Guoquan Yan, Formal analysis, Software; Jun Li, Resources; Hao Lai, Resources; Chunsheng Wang, Conceptualization, Supervision, Writing - review and editing,Resources; Kai Zhu, Conceptualization, Visualization, Supervision, Funding acquisition,Project administration, Writing - review and editing; Weijia Zhang, Conceptualization, Visualization, Supervision, Funding acquisition, Writing - original draft, Project administration, Writing - review and editing.

Competing Interest Statement

The authors declare no competing interest.

Funding

This work was supported by grants from the National Key R&D Program of China (2018YFC1005002), the National Natural Science Foundation of China (82070482, 81771971, 81772007, 21734003, and 51927805), the Shanghai Municipal Science and Technology Major Project (Grant No. 2017SHZDZX01), the Science and Technology Commission of Shanghai Municipality (17JC1400200, 20ZR1411700), and the Shanghai Municipal Education Commission (Innovation Program 2017-01-07-00-07-E00027).

Availability of data and materials

All the data associated with this study are included in the paper or Supplementary Files. The mass spectrometry proteomics data, including raw data from the mass spectrometry runs, have been deposited to the ProteomeXchange Consortium via the PRIDE partner repository with the dataset identifier PXD026303. The analyzed data are reported in Figure1 and Figure 1—source data 2-4.

Ethics

Human aortic samples were collected from patients who underwent ascending aorta surgery at Zhongshan Hospital, Fudan University. Written informed consent was obtained from all patients before participation. Human aortic specimens were utilized under approvals of Zhongshan Hospital, Fudan University Ethics Committee (NO. B2020-158).

Supplementary File

779 The Supplementary File include the following:
780 Uncropped images of western blotting.
781 Online Tables I-VI

782 **References**

783 **Akazawa Y**, Motoki N, Tada A, Yamazaki S, Hachiya A, Matsuzaki S, Kamiya M, Nakamura T,
784 Kosho T, and Inaba Y. 2016. Decreased aortic elasticity in children with Marfan syndrome or
785 Loeys-Dietz syndrome. *Circulation Journal* **80**: 2369-2375. DOI: 10.1253/circj.CJ-16-0739, PMID:
786 27733734
787 **Balistreri CR**, Crapanzano F, Schirone L, Allegra A, Pisano C, Ruvolo G, Forte M, Greco E,
788 Cavarretta E, Marullo AGM*, et al.* 2018. Deregulation of Notch1 pathway and circulating
789 endothelial progenitor cell (EPC) number in patients with bicuspid aortic valve with and without
790 ascending aorta aneurysm. *Scientific Reports* **8**: 13834. DOI: 10.1038/s41598-018-32170-2,
791 PMID: 30218064
792 **Bell V**, Mitchell WA, Sigurðsson S, Westenberg JJM, Gotal JD, Torjesen AA, Aspelund T, Launer
793 LJ, de Roos A, Gudnason V*, et al.* 2014. Longitudinal and circumferential strain of the proximal
794 aorta. *Journal of the American Heart Association* **3**: e001536. DOI: 10.1161/JAHA.114.001536,
795 PMID: 25523153
796 **Chen K-H**, Guo X, Ma D, Guo Y, Li Q, Yang D, Li P, Qiu X, Wen S, Xiao R-P*, et al.* 2004.
797 Dysregulation of HSG triggers vascular proliferative disorders. *Nature Cell Biology* **6**: 872-883.
798 DOI: 10.1038/ncb1161, PMID: 15322553
799 **Chen L**, Zhang J, Lyu Z, Chen Y, Ji X, Cao H, Jin M, Zhu J, Yang J, Ling R*, et al.* 2018. Positive
800 feedback loop between mitochondrial fission and Notch signaling promotes survivin-mediated
801 survival of TNBC cells. *Cell death & disease* **9**: 1050. DOI: 10.1038/s41419-018-1083-y, PMID:
802 30323195
803 **Coady MA**, Ikonomidis JS, Cheung AT, Matsumoto AH, Dake MD, Chaikof EL, Cambria RP,
804 Mora-Mangano CT, Sundt TM, and Sellke FW. 2010. Surgical management of descending
805 thoracic aortic disease: open and endovascular approaches. *Circulation* **121**: 2780-2804. DOI:
806 10.1161/CIR.0b013e3181e4d033, PMID: 20530003
807 **Cooper HA**, Cicalese S, Preston KJ, Kawai T, Okuno K, Choi ET, Kasahara S, Uchida HA, Otaka
808 N, Scalia R*, et al.* 2020. Targeting mitochondrial fission as a potential therapeutic for abdominal
809 aortic aneurysm. *Cardiovascular research* **117**: 971-982. DOI: 10.1093/cvr/cvaa133, PMID:
810 32384150
811 **Eckhouse SR**, Logdon CB, Oelsen JM, Patel RK, Rice AD, Stroud RE, Wince WB, Mukherjee R,
812 Spinale FG, Ikonomidis JS*, et al.* 2013. Reproducible porcine model of thoracic aortic aneurysm.
813 *Circulation* **128**: S186-93. DOI: 10.1161/CIRCULATIONAHA.112.000363, PMID: 24030405
814 **Garg V**, Muth AN, Ransom JF, Schluterman MK, Barnes R, King IN, Grossfeld PD, and
815 Srivastava D. 2005. Mutations in NOTCH1 cause aortic valve disease. *Nature* **437**: 270-274. DOI:
816 10.1038/nature03940, PMID: 16025100
817 **Goldfinger JZ**, Halperin JL, Marin ML, Stewart AS, Eagle KA, and Fuster V. 2014. Thoracic
818 aortic aneurysm and dissection. *Journal of the American College of Cardiology* **64**: 1725-1739.
819 DOI: 10.1016/j.jacc.2014.08.025, PMID: 25323262
820 **Harrison OJ**, Torrens C, Salhiyyah K, Modi A, Moorjani N, Townsend PA, Ohri SK, and
821 Cagampang F. 2019. Defective NOTCH signalling drives smooth muscle cell death and
822 differentiation in bicuspid aortic valve aortopathy. *European Journal of Cardio-Thoracic Surgery*
823 **56**: 117-125. DOI: 10.1093/ejcts/ezy464, PMID: 30689881
824 **Herrington DM**, Mao C, Parker SJ, Fu Z, Yu G, Chen L, Venkatraman V, Fu Y, Wang Y, Howard
825 TD*, et al.* 2018. Proteomic architecture of human coronary and aortic atherosclerosis. *Circulation*
826 **137**: 2741-2756. DOI: 10.1161/CIRCULATIONAHA.118.034365, PMID: 29915101
827 **High FA**, Zhang M, Proweller A, Tu L, Parmacek MS, Pear WS, and Epstein JA. 2007. An
828 essential role for Notch in neural crest during cardiovascular development and smooth muscle
829 differentiation. *The Journal of Clinical Investigation* **117**: 353-363. DOI: 10.1172/JCI30070, PMID:
830 17273555
831 **Hofemeier AD**, Limon T, Muenker TM, Wallmeyer B, Jurado A, Afshar ME, Ebrahimi M,
832 Tsukanov R, Oleksiievets N, Enderlein J, Gilbert PM, Betz T. 2021. Global and local tension

measurements in biomimetic skeletal muscle tissues reveals early mechanical homeostasis. *Elife* **10**:e60145. DOI: 10.7554/eLife.60145, PMID: 33459593

Ikonomidis JS, Gibson WC, Gardner J, Sweterlitsch S, Thompson RP, Mukherjee R, and Spinale FG. 2003. A murine model of thoracic aortic aneurysms. *Journal of Surgical Research* **115**: 157-163. DOI: 10.1016/s0022-4804(03)00193-8, PMID: 14572787

Ingber DE. 2016. Reverse engineering human pathophysiology with organs-on-chips. *Cell* **164**: 1105-1109. DOI: 10.1016/j.cell.2016.02.049, PMID: 26967278

Isselbacher EM, Lino Cardenas CL, and Lindsay ME. 2016. Hereditary influence in thoracic aortic aneurysm and dissection. *Circulation* **133**: 2516-2528. DOI: 10.1161/CIRCULATIONAHA.116.009762, PMID: 27297344

Kasahara A, Cipolat S, Chen Y, Dorn GW, and Scorrano L. 2013. Mitochondrial fusion directs cardiomyocyte differentiation via calcineurin and notch signaling. *Science* **342**: 734-737. DOI: 10.1126/science.1241359, PMID: 24091702

Koenig SN, LaHaye S, Feller JD, Rowland P, Hor KN, Trask AJ, Janssen PM, Radtke F, Lilly B, Garg V. 2017. Notch1 haploinsufficiency causes ascending aortic aneurysms in mice. *JCI Insight* **2**:e91353. DOI: 10.1172/jci.insight.91353, PMCID: PMC5752295

Li Y, Ren P, Dawson A, Vasquez HG, Ageedi W, Zhang C, Luo W, Chen R, Li Y, Kim S*, et al.* 2020. Single-cell transcriptome analysis reveals dynamic cell populations and differential gene expression patterns in control and aneurysmal human aortic tissue. *Circulation* **142**: 1374-1388. DOI: 10.1161/CIRCULATIONAHA.120.046528, PMID: 33017217

Lindeman JH, and Matsumura JS. 2019. Pharmacologic management of aneurysms. *Circulation research* **124**: 631-646. DOI: 10.1161/CIRCRESAHA.118.312439, PMID: 30763216

Malashicheva A, Kostina A, Kostareva A, Irtyuga O, Gordeev M, and Uspensky V. 2020. Notch signaling in the pathogenesis of thoracic aortic aneurysms: A bridge between embryonic and adult states. *Biochimica et biophysica acta Molecular basis of disease* **1866**: 165631. DOI: 10.1016/j.bbadis.2019.165631, PMID: 31816439

Mao N, Gu T, Shi E, Zhang G, Yu L, and Wang C. 2015. Phenotypic switching of vascular smooth muscle cells in animal model of rat thoracic aortic aneurysm. *Interactive CardioVascular and Thoracic Surgery* **21**: 62-70. DOI: 10.1093/icvts/ivv074, PMID: 25829166

Michelena HI, Khanna AD, Mahoney D, Margaryan E, Topilsky Y, Suri RM, Eidem B, Edwards WD, Sundt TM, 3rd, and Enriquez-Sarano M. 2011. Incidence of aortic complications in patients with bicuspid aortic valves. *JAMA* **306**: 1104-1112. DOI: 10.1001/jama.2011.1286, PMID: 21917581

Miret-Casals L, Sebastián D, Brea J, Rico-Leo EM, Palacín M, Fernández-Salguero PM, Loza MI, Albericio F, and Zorzano A. 2018. Identification of new activators of mitochondrial fusion reveals a link between mitochondrial morphology and pyrimidine metabolism. *Cell Chemical Biology* **25**: 268-278.e264. DOI: 10.1016/j.chembiol.2017.12.001, PMID: 29290623

Morrison TM, Choi G, Zarins CK, and Taylor CA. 2009. Circumferential and longitudinal cyclic strain of the human thoracic aorta: age-related changes. *Journal of Vascular Surgery* **49**: 1029-1036. DOI: 10.1016/j.jvs.2008.11.056, PMID: 19341890

Noseda M, Fu Y, Niessen K, Wong F, Chang L, McLean G, and Karsan A. 2006. Smooth muscle alpha-actin is a direct target of Notch/CSL. *Circulation research* **98**: 1468-1470. DOI: 10.1161/01.RES.0000229683.81357.26, PMID: 16741155

Oller J, Gabandé-Rodríguez E, Ruiz-Rodriguez MJ, Desdín-Micó G, Aranda JF, Rodrigues-Diez R, Ballesteros-Martínez C, Blanco EM, Roldan-Montero R, Acuña P, Forteza Gil A, Martín-López CE, et al. 2021. Extracellular tuning of mitochondrial respiration leads to aortic aneurysm. *Circulation*. DOI: 10.1161/CIRCULATIONAHA.120.051171, PMID: 33709773.

Olsson C, Thelin S, Ståhle E, Ekbom A, and Granath F. 2006. Thoracic aortic aneurysm and dissection: increasing prevalence and improved outcomes reported in a nationwide population-based study of more than 14,000 cases from 1987 to 2002. *Circulation* **114**: 2611-2618. DOI: 10.1161/CIRCULATIONAHA.106.630400, PMID: 17145990

Park SE, Georgescu A, and Huh D. 2019. Organoids-on-a-chip. *Science* **364**: 960-965. DOI: 10.1126/science.aaw7894, PMID: 31171693

Petsophonsakul P, Furmanik M, Forsythe R, Dweck M, Schurink GW, Natour E, Reutelingsperger C, Jacobs M, Mees B, and Schurgers L. 2019. Role of vascular smooth muscle cell phenotypic switching and calcification in aortic aneurysm formation. *Arteriosclerosis, Thrombosis, and Vascular Biology* **39**: 1351-1368. DOI: 10.1161/ATVBAHA.119.312787, PMID: 31144989

Prakash SK, Bossé Y, Muehlschlegel JD, Michelena HI, Limongelli G, Della Corte A, Pluchinotta FR, Russo MG, Evangelista A, Benson DW*, et al.* 2014. A roadmap to investigate the genetic basis of bicuspid aortic valve and its complications: insights from the International BAVCon (Bicuspid Aortic Valve Consortium). *Journal of the American College of Cardiology* **64**: 832-839. DOI: 10.1016/j.jacc.2014.04.073, PMID: 25145529

Salabei JK, and Hill BG. 2013. Mitochondrial fission induced by platelet-derived growth factor regulates vascular smooth muscle cell bioenergetics and cell proliferation. *Redox Biology* **1**: 542-551. DOI: 10.1016/j.redox.2013.10.011, PMID: 24273737

Sciacca S, Pilato M, Mazzoccoli G, Pazienza V, and Vinciguerra M. 2013. Anti-correlation between longevity gene SirT1 and Notch signaling in ascending aorta biopsies from patients with bicuspid aortic valve disease. *Heart and Vessels* **28**: 268-275. DOI: 10.1007/s00380-012-0238-5, PMID: 22370592

Shao S, Zhao X, Zhang X, Luo M, Zuo X, Huang S, Wang Y, Gu S, and Zhao X. 2015. Notch1 signaling regulates the epithelial-mesenchymal transition and invasion of breast cancer in a Slug-dependent manner. *Molecular cancer* **14**: 28. DOI: 10.1186/s12943-015-0295-3, PMID: 25645291

Thacker VV, Dhar N, Sharma K, Barrile R, Karalis K, McKinney JD. 2020. A lung-on-chip model of early Mycobacterium tuberculosis infection reveals an essential role for alveolar epithelial cells in controlling bacterial growth. *Elife* **9**:e59961. DOI: 10.7554/eLife.59961, PMID: 33228849

van der Pluijm I, Burger J, van Heijningen PM, A IJ, van Vliet N, Milanese C, Schoonderwoerd K, Sluiter W, Ringuette LJ, Dekkers DHW*, et al.* 2018. Decreased mitochondrial respiration in aneurysmal aortas of Fibulin-4 mutant mice is linked to PGC1A regulation. *Cardiovascular research* **114**: 1776-1793. DOI: 10.1093/cvr/cvy150, PMID: 29931197

Vasquez-Trincado C, Garcia-Carvajal I, Pennanen C, Parra V, Hill JA, Rothermel BA, and Lavandero S. 2016. Mitochondrial dynamics, mitophagy and cardiovascular disease. *The Journal of physiology* **594**: 509-525. DOI: 10.1113/JP271301, PMID: 26537557

Verma S, and Siu SC. 2014. Aortic dilatation in patients with bicuspid aortic valve. *New England Journal of Medicine* **370**: 1920-1929. DOI: 10.1056/NEJMra1207059, PMID: 24827036

Zhang B, Korolj A, Lai BF, Radisic M. 2018. Advances in organ-on-a-chip engineering. *Nature Reviews Materials* **3**:257–278. DOI: 10.1038/ s41578-018-0034-7.

Zhao Y, Rafatian N, Feric NT, Cox BJ, Aschar-Sobbi R, Wang EY, Aggarwal P, Zhang B, Conant G, Ronaldson-Bouchard K, Pahnke A, et al. 2019. A platform for generation of chamber-specific cardiac tissues and disease modeling. *Cell* **176**:913-927.e18. DOI: 10.1016/j.cell.2018.11.042, PMID: 30686581

Aorta-on-a-chip reveals impaired mitochondrial dynamics as a therapeutic target for aortic aneurysm in bicuspid aortic valve disease

Mieradilijiang Abudupataer[1], Shichao Zhu[1], Shiqiang Yan[2], Kehua Xu[2], Jingjing Zhang[2], Shaman Luo[2,3], Wenrui Ma[1], Md. Fazle Alam[2,3], Yuyi Tang[2], Hui Huang[2], Nan Chen[1], Li Wang[2], Guoquan Yan[2], Jun Li[1], Hao Lai[1], Chunsheng Wang[1]*, Kai Zhu[1]*, Weijia Zhang[1,2,3]*

[1] Department of Cardiac Surgery and Shanghai Institute of Cardiovascular Diseases, Zhongshan Hospital, Fudan University, Shanghai 200032, China; [2] Institutes of Biomedical Sciences, Shanghai Medical College, Fudan University, Shanghai 200032, China; [3] The State Key Laboratory of Molecular Engineering of Polymers, Fudan University, Shanghai 200438, China.

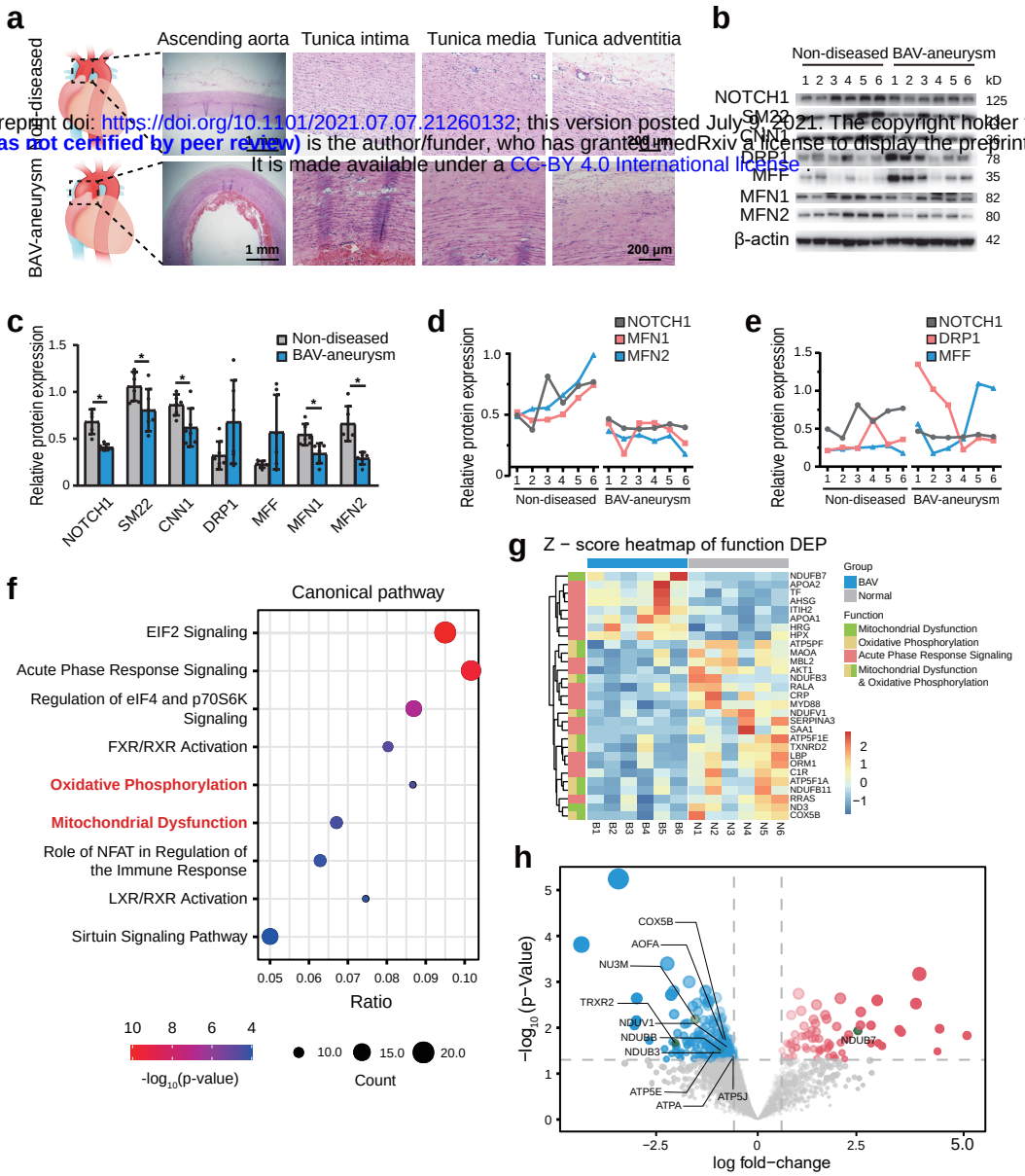

Figure 1. The relationship between NOTCH1 insufficiency and mitochondrial dysfunction in BAV-TAA. (**a**) H&E staining of non-diseased and BAV-TAA aortic tissues. The scale bar represents 1 mm in the low field and 200 μm in the high field. (**b**) Representative images of the western blotting analysis of the expression of NOTCH1, the mitochondrial dynamics proteins DRP-1, MFF, MFN1, and MFN2 and the contractile phenotype proteins SM22 and CNN1 in six non-diseased and six BAV-TAA aortic tissue fragments. (**c**) Quantification of the total band densities of the proteins normalized to the corresponding band density of β-actin (n = 6, **P* < 0.05, two-tailed Student's t tests were used between two groups). (**d**) Correlation analysis among the quantified protein expression levels of NOTCH1, MFN1 and MFN2. A positive correlation was found between NOTCH1 and MFN1 or MFN2 in aortic tissues. The R^2 between NOTCH1 and MFN2 was 0.8069, and that between NOTCH1 and MFN1 was 0.6137. (**e**) Correlation analysis between the quantified protein expression of NOTCH1 and DRP1 or MFF. No correlation was found. (**f**) The enriched canonical pathways were identified by IPA. Mass spectrometry-based comparative proteomics showed that mitochondrial dysfunction and the oxidative phosphorylation pathways were significantly enriched in BAV-TAA aortic tissues. (**g**) Heatmap of the expression of enriched proteins involved in mitochondrial dysfunction, the oxidative phosphorylation pathways and acute phase response signaling. (**h**) Volcano plot visualization of the differentially expressed proteins related to mitochondrial dysfunction. The colors indicate the following: gray, no differential expression; red, upregulated proteins; and blue, downregulated proteins. The proteins related to mitochondrial dysfunction are labeled. All the data are expressed as the means ± SDs.

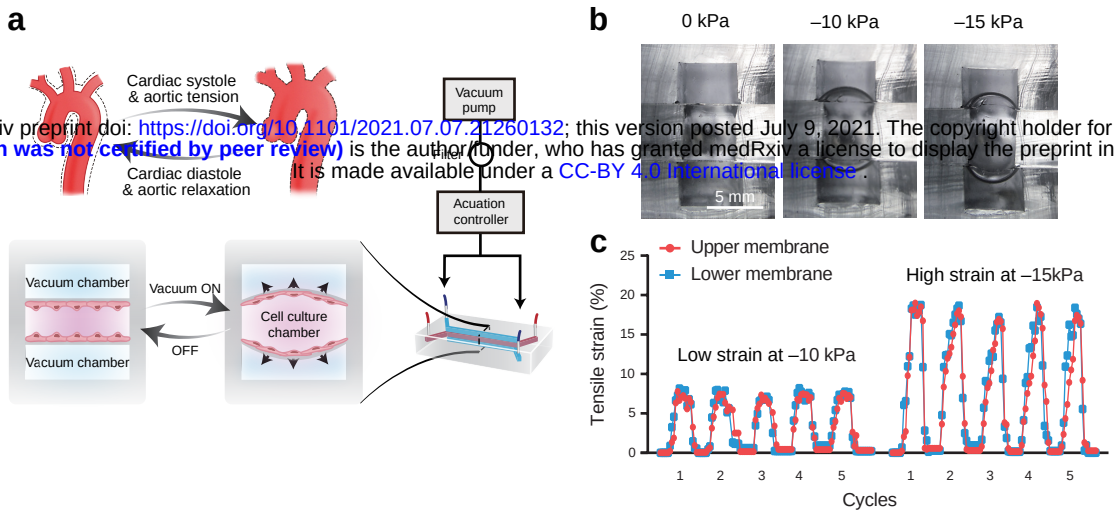

Figure 2. Schematic design and strain characterization of the aorta-on-a-chip model. (**a**) Schematic overview of the in vitro chip model. (**b**) Cross-sectional view of the microfluidic aorta-on-a-chip model showing the deformations of the PDMS membranes under different vacuum pressures. The scale bar represents 5 mm. (**c**) Measured tensile strains of the upper (red) and lower (blue) membranes at negative pressures of 10 kPa and 15 kPa for five cycles. The peak tensile strain per cycle averaged 7.18 ± 0.44% with a cyclic negative pressure of 10 kPa and 17.28 ± 0.91% with a cyclic negative pressure of 15 kPa.

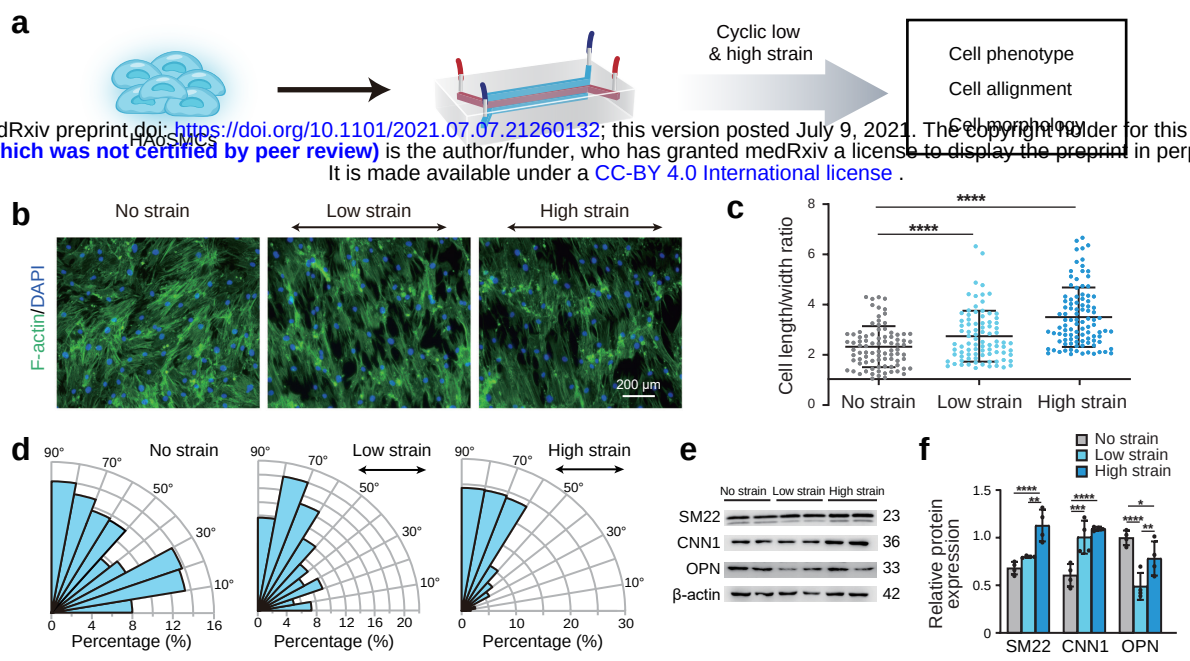

Figure 3. Effect of rhythmic strain on the cell morphology, alignment and phenotype. (**a**) Schematic workflow of cell culture on the chip model. (**b**) Representative images of cytoskeletal F-actin staining of HAoSMCs exposed to low or high rhythmic strain for 24 hrs. The scale bar represents 200 μm. (**c**) Length-to-width ratio of HAoSMCs after exposure to low or high rhythmic strain for 24 hrs. (n = 3, cells were measured in three fields per sample, ****P < 0.0001, one-way ANOVA followed by Tukey's post hoc test). (**d**) Alignments of HAoSMCs exposed to low or high rhythmic strain for 24 hrs. (**e**) Representative images of the western blotting analyses of protein markers of the contractile phenotype (SM22 and CNN1) and synthetic phenotype (OPN) of HAoSMCs after exposure to low or high rhythmic strain for 24 hrs. (**f**) Quantification of the total band densities for individual proteins normalized to the corresponding band of β-actin (n = 4, *P < 0.05, **P < 0.01, ***P < 0.001, ****P < 0.0001, one-way ANOVA followed by Tukey's post hoc test). All the data are expressed as the means ± SDs.

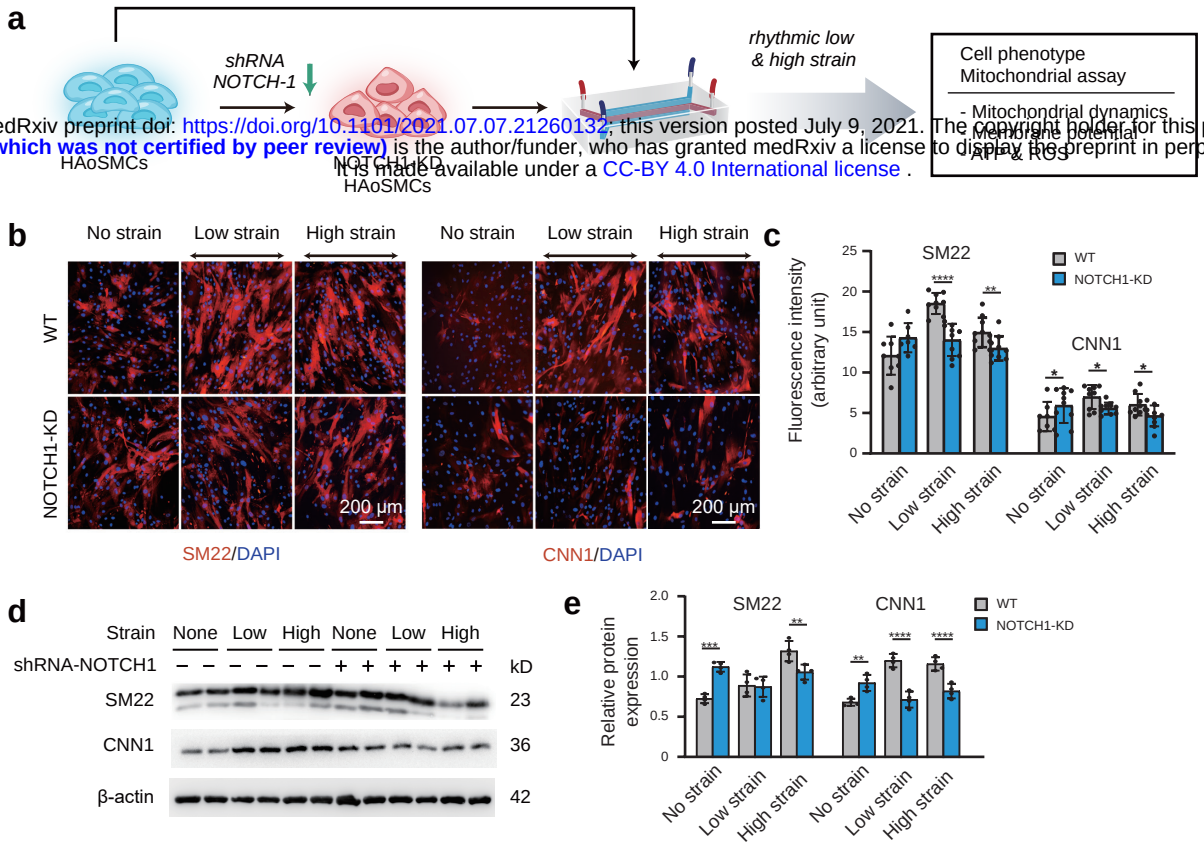

Figure 4. Phenotypic switching of NOTCH1-insufficient HAoSMCs under static and rhythmic strain conditions. (**a**) Schematic workflow of NOTCH1-KD HAoSMCs on the chip model. (**b**) Representative images of immunofluorescence staining of SM22 and CNN1 after exposure to rhythmic low or high strain for 24 hrs. The scale bar represents 200 μm. (**c**) Intensity of immunofluorescence staining of SM22 and CNN1 (**P* < 0.05, ***P* < 0.01, *****P* < 0.0001, two-way ANOVA followed by Tukey's post hoc test). (**d**) Representative images of the western blotting analyses of SM22 and CNN1 in the WT and NOTCH1-KD groups exposed to rhythmic low or high strains for 24 hrs. (**e**) Quantification of the total band densities for individual proteins normalized to the corresponding band density of β-actin (n = 4, ***P* < 0.01, ****P* < 0.001, *****P* < 0.0001, two-way ANOVA followed by Tukey's post hoc test). All the data are expressed as the means ± SDs.

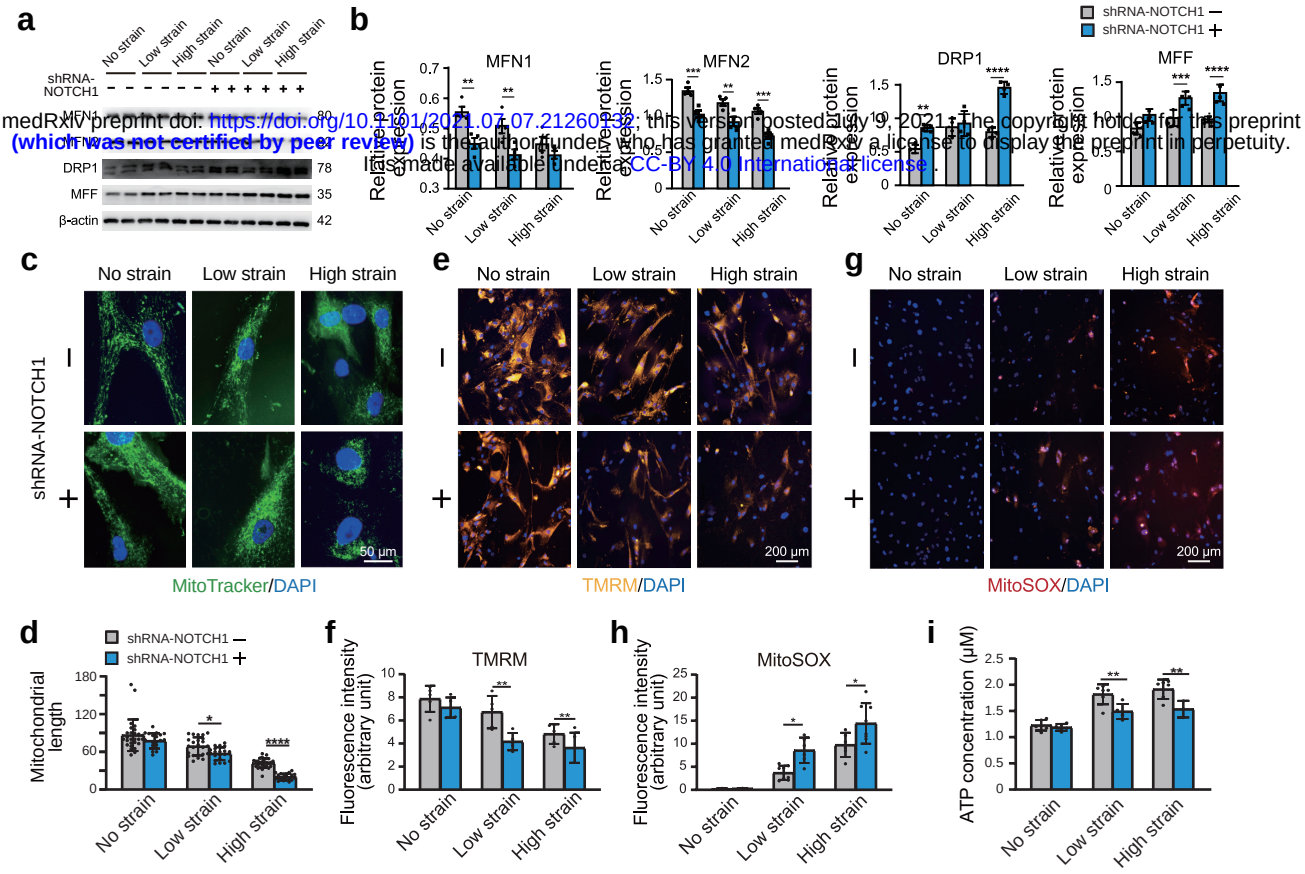

Figure 5. Effect of NOTCH1 insufficiency on mitochondrial dynamics and function in HAoSMCs. (**a**) Representative images of the western blotting analyses of MFN1, MFN2, DRP1 and MFF expression in the WT and NOTCH1-KD groups under rhythmic low or high strain or static conditions. (**b**) Quantification of the total band densities for four individual proteins normalized to the corresponding band density of β-actin (n = 4, **P* < 0.05, ***P* < 0.01, ****P* < 0.001, *****P* < 0.0001, two-way ANOVA followed by Tukey's post hoc test). (**c**) MitoTracker staining images of the mitochondrial morphologies in the WT and NOTCH1-KD groups under rhythmic low or high strain or static conditions. The scale bar represents 50 μm. (**d**) Quantification of the mitochondria length (n = 3, ***P* < 0.01, *****P* < 0.0001, two-way ANOVA followed by Tukey's post hoc test). (**e**) TMRM staining of the mitochondrial membrane potentials in the WT and NOTCH1-KD groups under rhythmic low or high strain or static conditions. The scale bar represents 100 μm. (**f**) Quantification of the relative TMRM fluorescence intensity (***P* < 0.01, two-way ANOVA followed by Tukey's post hoc test). (**g**) MitoSOX staining of mitochondrial superoxide generation in the WT and NOTCH1-KD groups. The scale bar represents 100 μm. (**h**) Quantification of the relative MitoSOX fluorescence intensity (**P* < 0.05, ***P* < 0.01, two-way ANOVA followed by Tukey's post hoc test). (**i**) The ATP concentrations were measured using an ATP Determination Kit (***P* < 0.01, two-way ANOVA followed by Tukey's post hoc test). Quantitative measurements were calculated using ImageJ software. All the data are expressed as the means ± SDs.

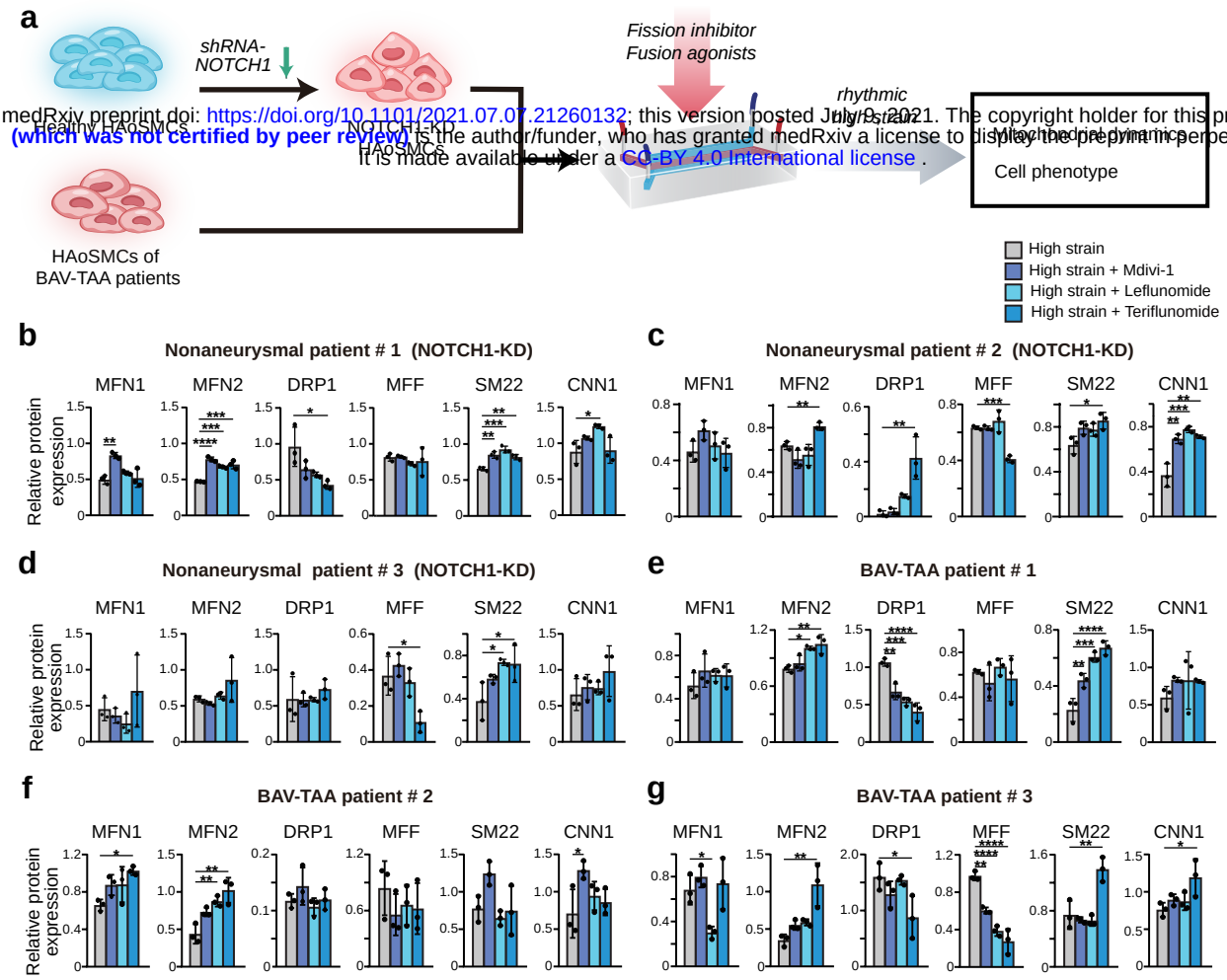

Figure 6. Screening of drugs that can rescue the cell phenotype and mitochondrial dynamics using the chip model. (**a**) Schematic workflow of the experimental design. After treatment with treated with Mdivi-1, leflunomide and teriflunomide on the chip models with (**b**) a NOTCH1-knockdown HAoSMC cell line (CRL1999), (**c**) NOTCH1-knockdown p-HAoSMCs isolated from non-diseased aortic tissues, (**d**) NOTCH1-knockdown p-HAoSMCs purchased from ATCC, and **(e-g)** p-HAoSMCs isolated from aortic tissues from three patients with BAV-TAA, quantification of the total band densities of the mitochondria-related proteins MFN1, MFN2, DRP-1, and MFF and the contractile phenotype proteins SM22 and CNN1 were normalized to the corresponding band densities of β-actin. All the data are expressed as the means ± SDs. n = 3, **P* < 0.05, ***P* < 0.01, ****P* < 0.001, *****P* < 0.0001, one-way ANOVA followed by Tukey's post hoc test.

Aorta-on-a-chip reveals impaired mitochondrial dynamics as a therapeutic target for aortic aneurysm in bicuspid aortic valve disease

Mieradilijiang Abudupataer[1], Shichao Zhu[1], Shiqiang Yan[2], Kehua Xu[2], Jingjing Zhang[2], Shaman Luo[2,3], Wenrui Ma[1], Md. Fazle Alam[2,3], Yuyi Tang[2], Hui Huang[2], Nan Chen[1], Li Wang[2], Guoquan Yan[2], Jun Li[1], Hao Lai[1], Chunsheng Wang[1]*, Kai Zhu[1]*, Weijia Zhang[1,2,3]*

[1] Department of Cardiac Surgery and Shanghai Institute of Cardiovascular Diseases, Zhongshan Hospital, Fudan University, Shanghai 200032, China; [2] Institutes of Biomedical Sciences, Shanghai Medical College, Fudan University, Shanghai 200032, China; [3] The State Key Laboratory of Molecular Engineering of Polymers, Fudan University, Shanghai 200438, China.

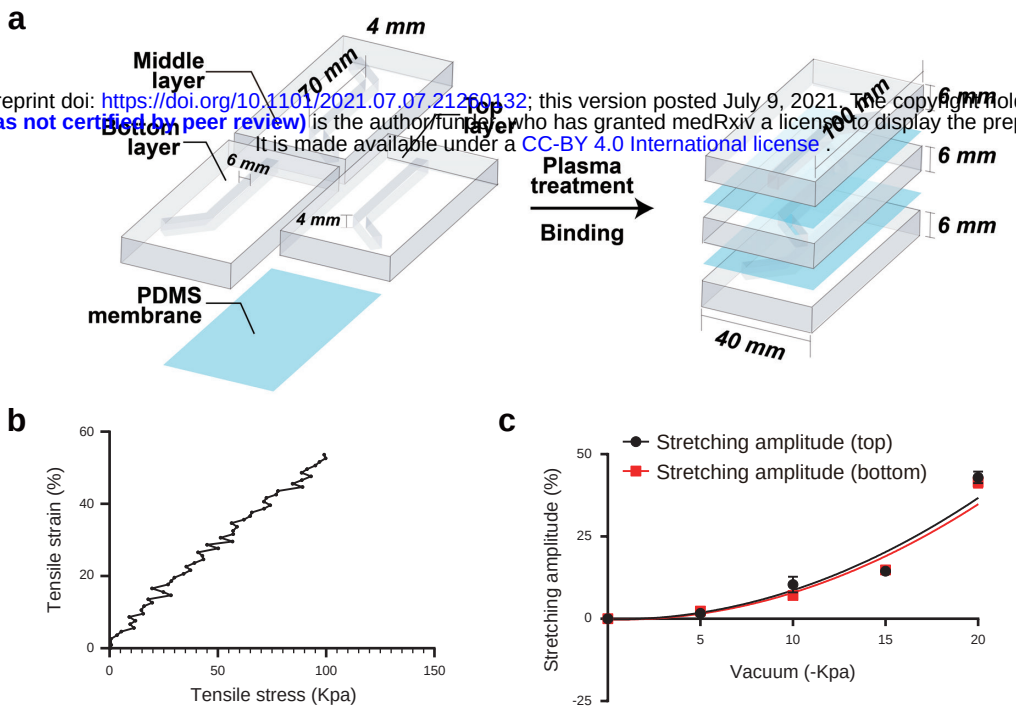

Figure 2—figure supplement 1. Characterization and parameters of the aorta-on-a-chip model. (**a**) Assembly and parameters of the PDMS aorta-on-a-chip model. (**b**) Young's modulus of the PDMS membrane. (**c**) Membrane deformation under different vacuum pressures (0 kPa, 10 kPa, 15 kPa and 20 kPa).

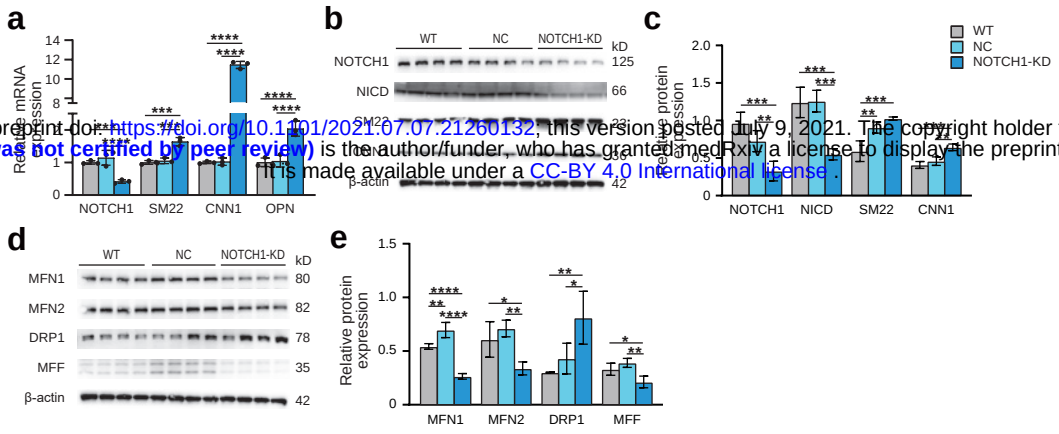

Figure 4—figure supplement 1. Alteration of NOTCH1 signaling, phenotype and mitochondrial dynamics in HAoSMCs after NOTCH1 shRNA transfection. (**a**) Expression of the NOTCH1, SM22, CNN1 and OPN1 genes in the NOTCH1-KD group compared with the group without virus (WT) and the negative control (NC) group by quantitative real-time PCR under static conditions. (**b**) Representative images of the western blotting analysis of NOTCH1, NICD, SM22 and CNN1 in the WT, NC and NOTCH1-KD groups under static conditions. (**c**) Quantification of the total band densities of individual proteins normalized to the corresponding band intensity of β-actin. **(d)** Representative images of the western blotting analysis of MFN1, MFN2, DRP1 and MFF in the WT, NC and NOTCH1-KD groups under static conditions. **(e)** Quantification of the total band densities of individual proteins normalized to the corresponding band density of β-actin. All the data are expressed as the means ± SDs. n = 3, **P < 0.05, **P < 0.01, ***P < 0.001, ****P < 0.0001,* one-way ANOVA followed by Tukey's post hoc test.

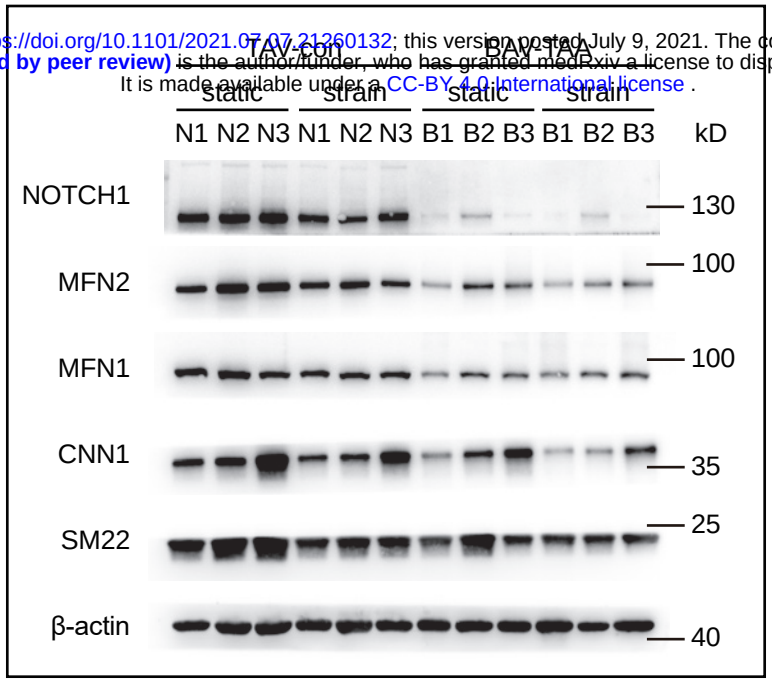

Figure 6—figure supplement 1. Expression of NOTCH1 and phenotype- and mitochondrial dynamics-related proteins in p-HAoSMCs from BAV-TAA aortic tissues. Image of the western blotting analysis of NOTCH1, the mitochondrial dynamics proteins MFN1 and MFN2 and the contractile phenotype proteins SM22 and CNN1 in primary HAoSMCs from BAV-TAA tissue with or without rhythmic strain.